A COMBINED CONFOCAL IMAGING AND RAMAN SPECTROSCOPY MICROSCOPE FOR IN VIVO SKIN CANCER DIAGNOSIS

by

Christopher Lyman Arrasmith

A thesis submitted in partial fulfillment
of the requirements for the degree

of

Master of Science

in

Electrical Engineering

MONTANA STATE UNIVERSITY
Bozeman, Montana

November, 2008

© Copyright

by

Christopher Lyman Arrasmith

2009

All Rights Reserved

APPROVAL

of a thesis submitted by

Christopher Lyman Arrasmith

This thesis has been read by each member of the thesis committee and has been found to be satisfactory regarding content, English usage, format, citations, bibliographic style, and consistency, and is ready for submission to the Division of Graduate Education.

Dr. David L. Dickensheets

Approved for the Department of Electrical and Computer Engineering

Dr. Robert C. Maher

Approved for the Division of Graduate Education

Dr. Carl A. Fox

STATEMENT OF PERMISSION TO USE

In presenting this thesis in partial fulfullment of the requirements for a master's degree at Montana State University, I agree that the Library shall make it available to borrowers under rules of the Library.

If I have indicated my intention to copyright this thesis by including a copyright notice page, copying is allowable only for scholarly purposes, consistent with "fair use" as prescribed in the U.S. Copyright Law. Requests for permission for extended quotation from or reproduction of this thesis in whole or in parts may be granted only by the copyright holder.

Christopher Lyman Arrasmith

November, 2008

DEDICATION

To the friends and family who have supported me in achieving this goal. Your motivation and support have been crucial to the realization of my goals in life, and continue to be a foundation for my future.

ACKNOWLEDGEMENTS

I would like to thank Dr. David Dickensheets for allowing me to take part in this project, for helping me improve my writing, technical and mathematical skills, and for all the advice and help he has given me along the way. His willingness to help with any and all problems I encountered is greatly appreciated. I would also like to thank: Marshall Overcast and Paul Nugent for their great help with MATLAB and ideas about improving the project, Amin Nehrir for allowing me to constantly bounce ideas off him, Eric Gowens for his help in developing the electrical components of the project as well as many other tasks, Chetan Patil for helping with the Raman Spectroscopy end of things, and Anita Mahadevan-Jansen for her support and collaboration on this project.

I would also like to express my appreciation to my family for helping me get through the past several years. They have provided motivation and support to finish that which I started, even through the rough spots.

Funding Acknowledgment

This work was kindly supported by the National Institutes of Health. However, any opinions, findings, conclusions, or recommendations expressed herein are those of the author(s) and do not necessarily reflect the views of NIH.

TABLE OF CONTENTS

1. INTRODUCTION 1

Raman Spectroscopy 2
Raman Spectroscopy and Confocal Microscopy Combined 3
Thesis Organization 5

2. INSTRUMENT OVERVIEW 7

Light Delivery and Collection 7
Microscope 10
Electronics and Control 14
Spectroscopy System 14

3. OPTICAL DESIGN 16

Optical Layout 16
Constraints 16
Path 18
Lens Choices 21
Optical Performance 24
Point Spread Function 24
Edge Response 27
Axial Response 27
Efficiency 31
Zemax Simulation 32
Telescope 32
Hemisphere front lens 35
CCD Imaging Setup 38
Opto-mechanical Considerations 40
Focus Control 41
Adjustment Methods 42

4. ELECTRONIC DESIGN AND USER INTERFACE 45

Amplifier Design 45
Image Formation 47
Focus Control 50
User Interface 51

TABLE OF CONTENTS – CONTINUED

5. RESULTS 54

Optical Performance 54
Edge Response 54
Axial Response 57
Imaging 59
Confocal Imaging 59
Large Area CCD 62
Raman Spectra 64

6. CONCLUSION 67

Future Work 67

REFERENCES CITED 69

LIST OF TABLES

Table Page

3.1 Objective lens properties 18

5.1 Measured edge response 56

5.2 Measured axial response 59

LIST OF FIGURES

Figure Page

1.1 Skin structure 5
2.1 Instrument subsystems 8
2.2 Laser 9
2.3 Light launch 10
2.4 Sketch of microscope design 12
2.5 Photos of the microscope 13
2.6 Raman spectrometer layout 15
3.1 MEMS scan mirror 17
3.2 Instrument subsystems 19
3.3 Large area preview techniques 20
3.4 Ideal fiber confocal optical microscope (FCOM) 25
3.5 Point spread function 26
3.6 Edge response 28
3.7 Axial response NA = 0.75 29
3.8 Axial response NA = 0.55 29
3.9 Axial FWHM vs. NA 30
3.10 Efficiency 31
3.11 Zemax telescope model 32
3.12 Telescope OPD 34
3.13 Hemisphere model layout 34
3.14 Hemisphere surface spot diagram 36
3.15 OPD fans for 50 μm depth 37
3.16 CCD imaging setup 38
3.17 CCD imaging spot diagram 39
3.18 Solidworks rendering 40

LIST OF FIGURES – CONTINUED

Figure Page

3.19 Attachment of front piece 44
4.1 Amplifier layout 46
4.2 Image formation and MEMS scan pattern 49
4.3 Image distortion correction 50
4.4 User interface 53
5.1 Edge response 55
5.2 Confocal channel axial response 58
5.3 Raman axial response and efficiency 60
5.4 Confocal imaging areas with available objective lenses 62
5.5 Confocal images of skin 63
5.6 CCD imaging comparison 64
5.7 Raman spectrum of normal skin 66

ABSTRACT

Confocal microscopy has provided a useful tool for imaging biopsied tissue samples. The cross sectioning ability inherent in confocal microscopes provides a method for viewing of cellular structure at different layers of a histology sample, allowing for optical cross sectioning and viewing structures below the surface of the sample. As a cancer diagnosis technique, confocal microscopy has been shown to provide valuable information showing differences in cell morphology of malignant and benign regions. Raman spectroscopy has also been shown to be a useful tool for cancer diagnosis in skin tissues due to its ability to distinguish different types of chemical bonds. While both of these methods may be used for cancer detection, current devices are limited to *ex vivo* samples. The goal of this project was to design and build a hand held microscope which could be used for *in vivo* confocal imaging and Raman spectroscopy of suspected malignant lesions in skin. This thesis describes the optical, mechanical and electrical design and fabrication of the microscope, as well as performance testing and initial *in vivo* skin data collected with the microscope. It is our hope that this instrument will be used to gather important *in vivo* skin cancer data and spur future developments in small diagnosis tools that can be used in a clinical setting.

INTRODUCTION

As one of the most common kinds of cancer in humans, skin cancer affected over one million Americans in 2007 [1]. Of the different types of skin cancer, basal cell carcinoma (BCC) is the most common and accounts for most new cancer cases. Somewhat less common but much more deadly is melanoma, which the American Cancer Society estimates had over 59,000 cases in 2007 [2]. Diagnosis of skin cancers begins with visual inspection, which may be aided by a magnifying glass or dermoscope. If the lesion in question is determined to be a possible cancer, a biopsy is taken. Diagnosis of the biopsy is done by a histologist, who reviews many characteristics of the biopsy to characterize the presence of and type of skin cancer. Difficulty in the visual diagnosis of skin cancers arises because of the visual similarity between many benign skin lesions and malignant cancers, leading to a correct visual diagnosis rate of 50% to 75% of both BCC and melanoma for experienced clinicians [3, 4]. This means that much of the time skin biopsies are taken when there is no need, adding both to the cost of diagnosis and discomfort for the patient. Instruments which help *in vivo* diagnosis of skin cancer would improve false positive rates and reduce cost because fewer biopsies would need to be performed, as well as increase patient comfort.

The dermoscope is the primary tool for visual inspection and initial diagnosis of skin cancers [5]. A dermoscope is essentially a hand held low power microscope allowing direct visual inspection or imaging of the lesion. Dermoscopes are similar to a magnifying glass, but with inbuilt illumination, higher, adjustable magnification, and often image recording capabilities. Typically, a dermoscope provides 10x magnification using an achromatic lens. Illumination is accomplished by halogen lamps or LEDs, which are placed at around a 20° angle with respect to the optical axis. Some dermoscopes provide variable lighting schemes which are achieved by turning on and

off different color LEDs, which may help to see features needed to characterize the skin lesion [5].

Raman Spectroscopy

The initial discovery of Raman scattering took place in 1928 by two scientists from India, Raman and Krishnan [6]. The experiment showing this type of scattering consisted of passing an intense beam of sunlight through a liquid sample and using filters to extinguish the illumination light. When a blue-violet filter and a yellow-green filter were placed into the incident light it was completely extinguished. However, with the blue-violet filter placed before and the yellow-green filter placed after the liquid, output light was seen. This light was initially set apart from fluorescence because of its relative feebleness compared with fluorescence and because its polarization was comparable with ordinary scattering [6].

The mechanism for Raman scattering is a change in the rotational or vibrational quantum state of the sample being illuminated. When light is incident on a sample most of the scattering that takes place is elastic with no loss of energy, and therefore no wavelength change. For particles smaller than the illumination wavelength, this is known as Rayleigh scattering and does not cause a change in wavelength of the incident light. Raman scattering is due to an inelastic scattering of incident photons whereby energy is transfered to or received from the sample due to a change in the vibrational or rotational modes of the molecule, causing a change in the energy, and therefore the wavelength of the scattered light. If the incident photon gives up energy to the sample it is scattered with a longer wavelength and referred to as a stokes shift. If the molecule is already in an excited energy state and gives energy to the scattered photon the output has a shorter wavelength and is referred to as anti-stokes shifted.

Because the probability of the molecule being in an excited state is much lower than being in a ground state, the anti-stokes shift is a much weaker effect. It is important to note that Raman scattering is much different from fluorescence, where the incoming photon is completely absorbed by the molecule and causes an electronic energy state change, to be released by the molecule as a fluorescence photon some time later [7].

The wavelengths of light that are scattered by a sample are unique to the available vibrational and rotational modes of the molecules in the sample, creating a chemical fingerprint that can be used to identify the molecular structure. This Raman spectrum consists of many sharp lines that are easily distinguishable from the broad fluorescence spectrum as well as spectra from different molecules. In Raman spectroscopy the Rayleigh light is first filtered out, then the relative energies of the Raman peaks are recorded and used for chemical identification.

Using Raman spectroscopy, the molecular structure of skin lesions can be identified and used to classify different types of cells, including cancers. Through the use of neural network classification algorithm, Raman spectroscopy has been used to correctly identify melanoma with 80.5% accuracy and BCC to 95.8%, accuracy which is better than the diagnosis rate of visual inspection by experienced dermatologists [1]. The ability of automated computer classification of skin cancers using Raman spectroscopy makes it ideal for incorporation into a cancer detection microscope.

Raman Spectroscopy and Confocal Microscopy Combined

The diagnosis of skin cancer is accomplished by histology: looking at the cell structure of thin slices of skin from a biopsy of the lesion. So, in developing a microscope for *in vivo* cancer diagnosis a method of doing a virtual histology of the skin needs to be implemented. Confocal microscopy is a powerful tool for looking

at cross sections of a sample, thereby creating a virtual histology of the layers of the skin. In a confocal microscope, light which is not at the focus of the objective lens is rejected from the image by a pinhole in the optical path. So the parts of the sample that would appear blurry in a standard microscope do not appear at all in a confocal setup, giving the ability to view portions of the sample that are only at the focal plane. Because of this cross sectioning ability, confocal microscopy has been used to study the morphology of living skin through the epidermis and into the dermis layer [8]. When compared with histology images, confocal images provide much of the same detail on cell structure and large cellular deformations, which can be used to diagnose cancers [9]. Because confocal imaging can be accomplished *in vivo*, information about the living tissue, such as blood flow, can be gathered, which is not available in a biopsy. While confocal imaging does not provide the same contrast as histological samples, especially when using a stain, it does provide a method for increasing the probability of correct diagnosis before a biopsy needs to be taken.

Combining the cross sectioning ability of a confocal microscope with the chemical identification aspects of Raman spectroscopy gives a powerful tool for *in vivo* skin cancer diagnosis. The confocal image not only gives information on cell morphology, but can be used to locate potentially malignant areas in which Raman spectra can be taken for further discrimination. This precision targeting of skin areas improves the ability of Raman spectroscopy to distinguish normal cells from potentially cancerous cells [8]. The confocal aspect of the Raman spectra obtained helps to localize the area from which Raman spectra are taken. As Caspers et al. have shown, confocal Raman microscopes have been used to find water concentrations in the epidermal and dermal skin layers with 5 μm depth resolution [10]. Since most skin cancers begin at the dermis-epidermis junction, the ability to resolve Raman features at this depth, which is around 100 μm below the surface, greatly improves the diagnosis

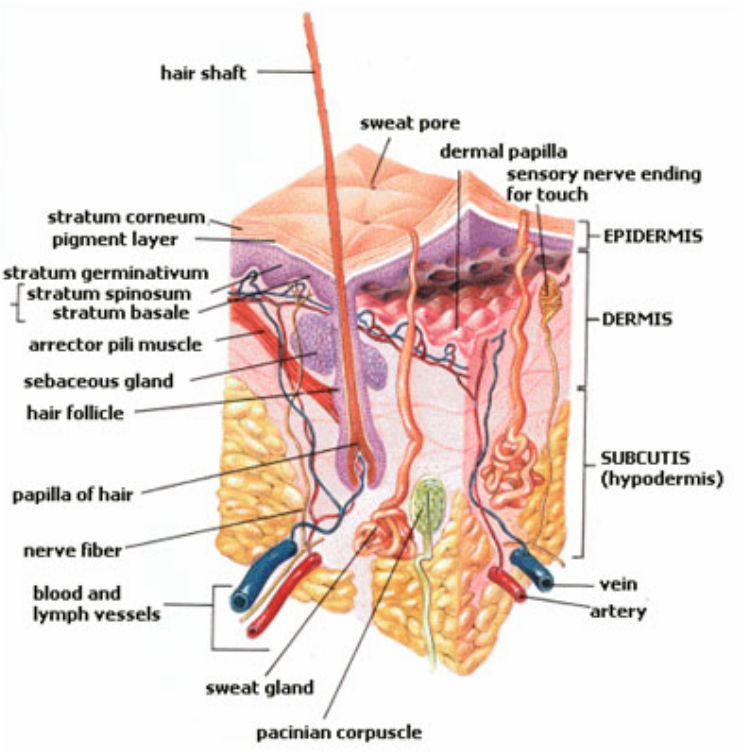


Figure 1.1: Structure of skin layers. Most cancers begin ad the epidermis-dermis junction, so it is necessary for a cancer diagnosis microscope to penetrate through the dermis [11].

ability of the microscope. Refer to Figure 1.1 for a rendering of skin structure. This thesis describes the design, fabrication, and characterization of the Confocal Imaging and Raman Spectroscopy Microscope (CIRSM) which was developed as a skin cancer diagnostic tool.

Thesis Organization

This thesis will discuss the design, fabrication and characterization of the confocal microscope. In chapter two, an overview of the instrument will be given discussing the various sub systems in the design. Chapter three describes the optical design including the optical layout, Zemax modeling and choice of lenses in the microscope. Chapter

four discusses control and user interface as well as the amplification scheme for light detection on the confocal channel. Results and sample images and Raman spectra are given in chapter five, and the conclusion in chapter six will discuss successes and necessary improvements for future development of this microscope.

INSTRUMENT OVERVIEW

Four sub-systems can be used to summarize the design and function of the confocal Raman microscope: the light delivery and collection, microscope probe, electronics and microscope control, and spectroscopy system. Because the microscope is designed for minimal size, the other systems are located on a remote computer station. This remote computer station includes a computer, fiber-coupled laser source, detector and amplification electronics, and the Raman spectrometer. Electronic and fiber optic connections allow communication and light delivery and collection to the hand-held unit, as seen in figure 2.1.

A brief overview of laser source and light launch will be discussed in the beginning of this chapter, then the optical layout for the microscope, followed by a description of the amplification electronics and control design and finally a description of the spectrometer used for Raman sampling.

Light Delivery and Collection

The CIRSM uses an 830 nm laser source for illumination and a fiber circulator for delivery and return of the laser light. The laser is a product of Sacher Lasertechnik and consists of an external cavity laser diode (ECDL) in a Littrow configuration. In this configuration, which is shown in figure 2.2 on page 9, collimated laser light is incident on a diffraction grating which feeds the first-order light back into the diode. The emission of the laser then comes out the rear facet of the diode where it is collimated[12]. The output of the laser is fiber coupled, providing ease of integration for the fiber circulator used for light delivery and collection, which is the core of the light launch system. Typical single port light launch and detection systems would

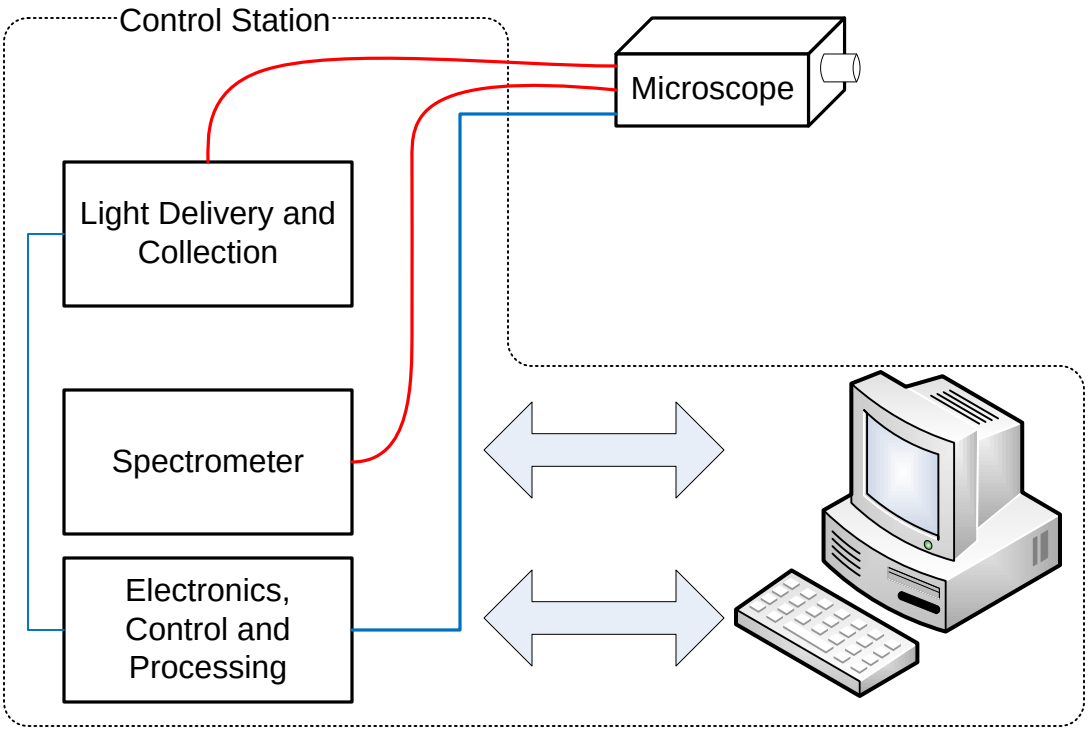


Figure 2.1: Block diagram of instrument subsystems. Curved red lines represent optical connections while straight blue lines represent electrical connections.

require external beam splitters to separate incoming and reflected light. Instead, fiber circulators utilize a combination of the Faraday effect and polarizers to separate the different propagation directions and couple them to different ports on the device. The circulator used in this design is polarization dependent, so care must be taken to launch laser light into the correct polarization axis of the fiber on port 1 of the circulator to maximize efficiency. Input light comes out port 2, which is connected to a fiber collimator on the rear of the microscope. Reflected light from the sample is coupled back into the fiber on port 2 via the same collimator, and transmitted to port 3 of the fiber circulator, which is connected to an avalanche photodiode (APD) for detection. Figure 2.3 depicts the light delivery and collection for both the confocal and Raman channels.

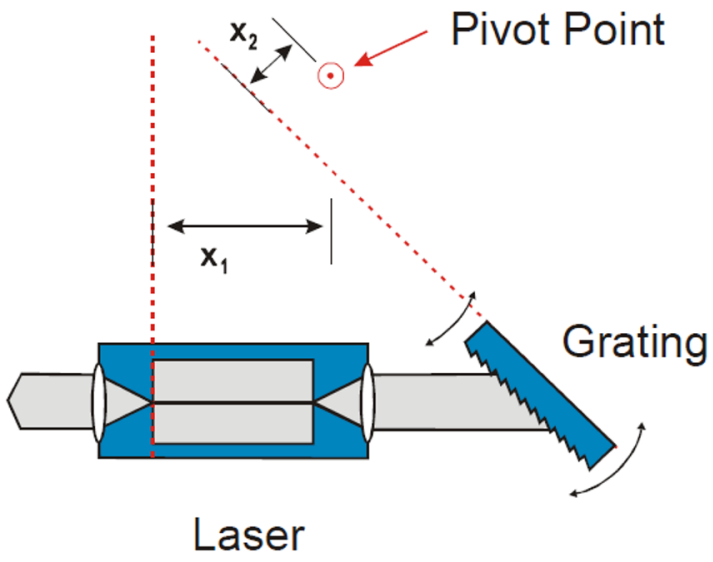


Figure 2.2: Modified Littrow configuration used in laser source from Sacher Lasertechnik [12].

During initial testing of the microscope, a problem with noise in the image was noticed and found to be caused by interference noise in the output intensity from port 3 of the circulator. The noise was noticed without port 2 being connected to the microscope, and we hypothesized that it was due to internal reflections within the circulator interfering with reflections from the fiber end face on port 2. Our solution was to place a $\lambda/4$ wave plate into the light path just before light enters the objective lens of the microscope, so light reflected from the sample has a polarization axis 90° from the incoming light due to a double pass through the wave plate. We then rotated the polarization state of the laser light 90° from the preferred axis of port 1 so any light reflected internally in the circulator would not be coupled to port 3. The wave plate changes the polarization of the light reflected from the sample to match the preferred mode input on port 2 so maximum reflected light is collected. Coupling into the wrong polarization mode in port 1 of the circulator produces an

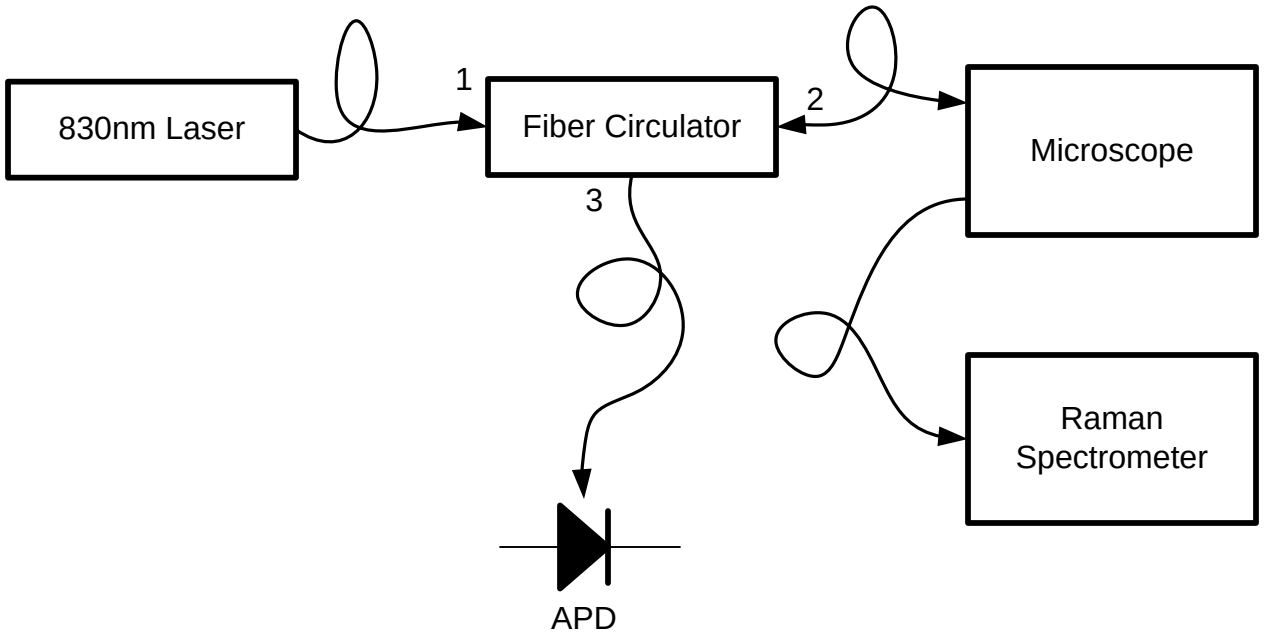


Figure 2.3: Light launch for fiber confocal optical microscope using a fiber circulator to distinguish illumination and reflected light.

output power loss of about 65% seen at port 2. However, the absence of the noise seen without this procedure provides better imaging, even considering the power loss.

The microscope uses a second fiber channel for collection of the Raman scattered light, the methods for which will be discussed in the next section. The fiber for the Raman channel is connected directly to the Raman spectrometer. The spectroscopy section at the end of this chapter will provide more detail on this setup.

Microscope

A sketch of the microscope layout can be referred to in Figure 2.4. After entering through the collimation adapter on the rear of the microscope, the collimated light

then passes through the filter block consisting of a laser cleanup filter, dichroic mirror, and long-pass Raman filter. Next, it is incident on the MEMS scan mirror, which provides two-axis scanning of the laser beam. This MEMS mirror is the heart of the miniature design of the CIRSM due to its size reduction compared with galvanometer based scanning systems used in bench top microscopes. Telescope lenses then provide a magnification of 3x to ensure the laser beam fills the rear aperture of the objective lens as well as imaging the MEMS mirror into the rear aperture of the objective lens. Just after the telescope lens in the optical path is the optional quarter wave plate used to provide 90° polarization rotation to the reflected light for the interference noise reduction scheme described previously, and a beam splitter used to pick off some of the return light and provide a large-area image to the CCD board camera. The CIRSM was designed to accommodate two objective lenses to provide variability in the numerical aperture (NA) for image quality testing. The interface between the front of the objective lens and the sample consists of an exchangeable front piece with either a clear aperture or a hemisphere lens. The hemisphere lens is used to provide an additional increase in NA and give more variability in imaging options. Focus control is accomplished by translating the objective lens, which is mounted on a linear translation stage. As seen in figure 2.4 a threaded picomotor (New Focus) actuator is used to move the translation stage. This actuator has the ability for manual adjustment or electronic control.

The laser light that forms the confocal image retraces the same route and is couple into the same fiber on port 2 of the circulator. Two LEDs mounted just in front of the objective lens provide additional white light for the large-area CCD camera image. After returning through the objective lens, the beam splitter mentioned before reflects a small amount (∼5 %) of the light toward the CCD camera. A 1:1 imaging system

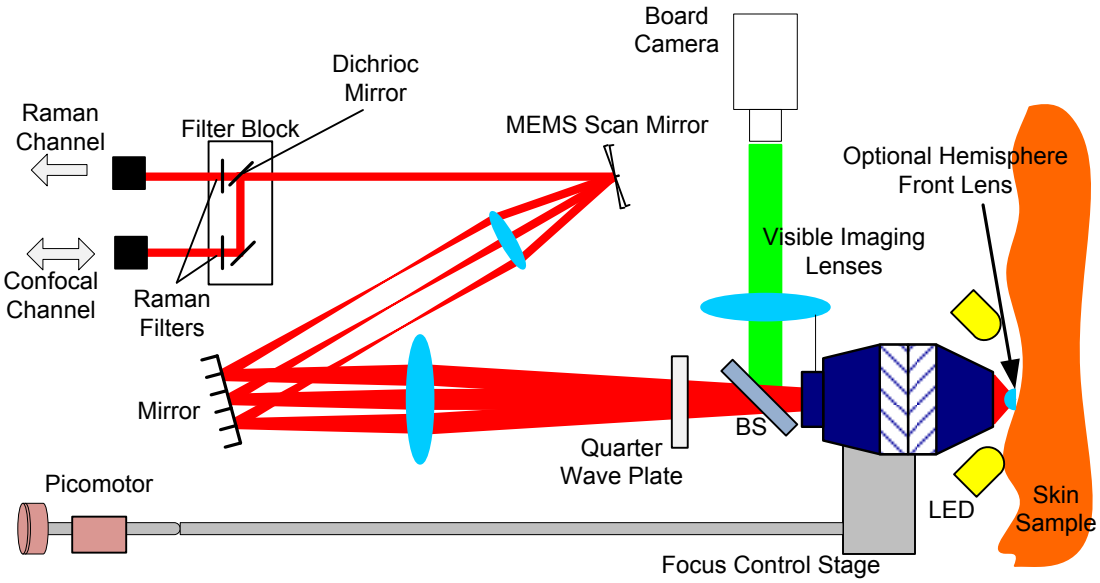


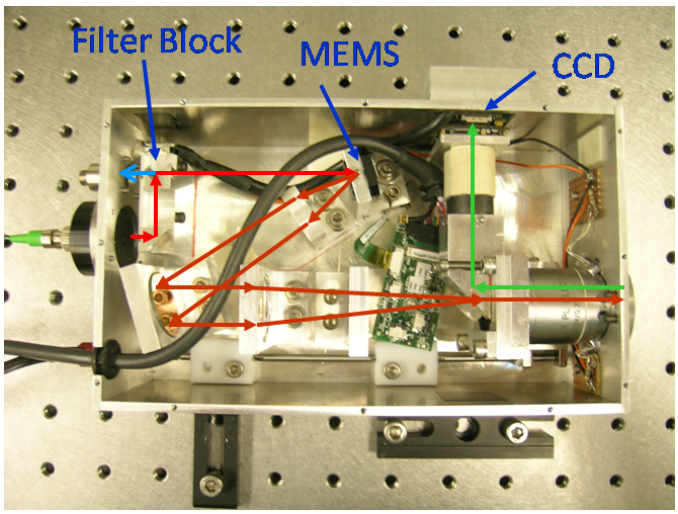
Figure 2.4: Sketch of microscope

focuses this light onto the camera detector. Figure 2.5 contains two photos of the finished microscope showing the top view and light path, as well as a side view.

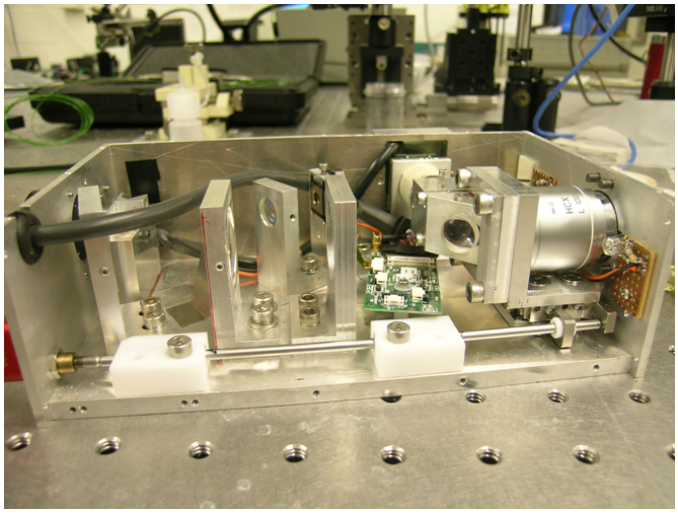
Light that is generated by Raman scattering is coupled back through the objective lens and traces the incoming optical path until it reaches the dichrioc mirror, where the stokes-shifted light passes through the dichroic and laser cleanup filter and is coupled into a multi-mode fiber via a second fiber adapter. The cleanup filter is a long-pass filter which blocks any laser light that may leak through the dichroic mirror.

The large-area image produced by the CCD board camera was designed to simplify locating small features on the skin surface and aligning the confocal image with these features. Initially we thought a method of routing the large-area image to the CCD camera in front of the objective lens could be developed, which was the reason for the choice of long working distance objective lenses, as shown in the next chapter. However, after investigating several methods of imaging in front of the objective lens

we found there was no adequate method for doing this, and decided to gather the large-area image through the objective lens. This decreased the performance of the microscope slightly because some of the laser light is lost at the beam splitter used to reflect the large-area image to the CCD camera. The investigated methods as well as the eventual design for the large-area image will be presented in the following chapter.



(a)



(b)

Figure 2.5: View of the top of the microscope showing the optical paths (a) and the side of the microscope (b)

Electronics and Control

Confocal image formation is accomplished with a combination of an APD detector (Hamamatsu), analog amplifier, and image acquisition (IMAQ) card (National Instruments). Because the APD does not necessarily output voltage levels that fit the input levels of the IMAQ card, an analog amplifier was designed to interface between the two devices. The design of the amplifier also allows for either linear or logarithmic amplification, the latter providing better imaging of skin due to a boost in small signal gain. Another useful element of the analog design is the ability to adjust the black reference level of the image, which allows the user to truncate noise visible in images. The interface with the IMAQ card also required a frame start signal and line start signal for image creation. These two signals are relayed from the MEMS controller and buffered in the amplifier circuit before being sent to the IMAQ card.

The picomotor actuator used for focus control is connected to a network controller allowing the computer to control motor movement using a TCPIP interface. The CCD camera used to provide a large-area view of the sample requires a USB connection to the computer.

The user interface for controlling the CIRSM and image processing was developed in the Labview environment. Live confocal video and color large-area video are visible simultaneously, with the ability for frame and video capture. This interface also allows the user to adjust the focus of the microscope.

Spectroscopy System

The Raman spectrometer used to interface with the CIRSM is a holographic imaging spectrometer manufactured by Kaiser Optical Systems. In this system, seen

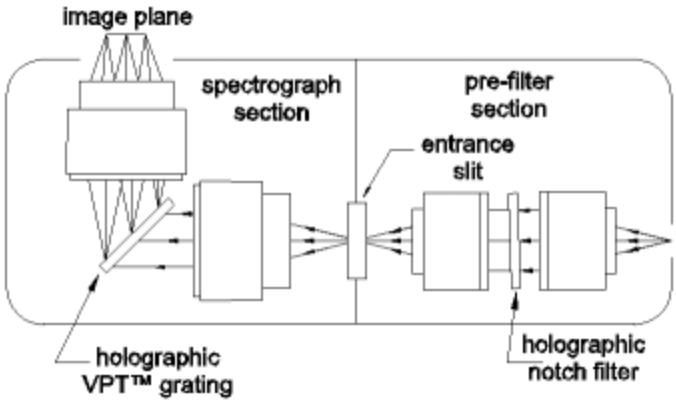


Figure 2.6: Layout of the Holospec f/1.8i Holographic Imaging Spectrograph used for Raman spectroscopy [13].

in figure 2.6, a holographic grating is used to separate the wavelengths of incoming light which are then focused onto a cooled CCD camera. The position of the light on the CCD corresponds to the wavelength. The camera is a TE-cooled deep depletion CCD camera from Princeton Instruments. Deep depletion cameras are designed to offset the decrease in quantum efficiency of silicon sensors for NIR wavelengths and give increased response over conventional CCD cameras for the NIR.

Raman light separated from the illumination light by the dichrioc mirror and cleaned by the long pass filter is relayed to the spectrometer by a multi-mode fiber. The fiber core diameter corresponds directly to the collection efficiency of the Raman channel, so larger fibers are needed to minimize integration time. However, as the core size of the fiber is increased, a larger sample volume is effectively being integrated and confocal sectioning is decreased. Experimentally a 50 μm-core fiber provided the best balance between collection efficiency and axial resolution of the Raman channel.

OPTICAL DESIGN

In the design of a confocal laser scanning microscope (CLSM) several key elements are necessary to obtain a confocal image and reject out-of-focus light. These elements include point illumination, point detection, and a scanning method to move the point of light across a sample [14]. In many microscopes, point detection is achieved by placing a pinhole in the return optical path to spatially filter out of focus light. In the CLSM described in this project an optical fiber provides the pinhole for both the point illumination and detection, since the same fiber is used for both illumination and return paths. Scanning is achieved in this design by a MEMS two-dimensional scan mirror to raster the laser beam across the sample. This chapter will first detail the optical layout and design constraints for the CIRSM, including trial methods for the large area preview. Next, theoretical performance measurements and optical simulations using Zemax optical design software will be developed. Finally, the opto-mechanical design and considerations will be described.

Optical Layout

Constraints

Because of the desire for variable NA in the CLSM, strict values for the field of view were not set. However, a field of view between 200 and 500 microns with a spatial resolution of one micron would allow for viewing of cell morphology at lower NA and cell structure at higher NA. The elements that constrain the optical design are the size of the MEMS scan mirror, the rear aperture diameter of the two objective lenses, and the need for a live preview of a large sample area using a CCD camera. The constraints due to the diameter of the MEMS scan mirror and the rear aperture of the objective lenses directly affect lens choices for the telescope portion of the microscope

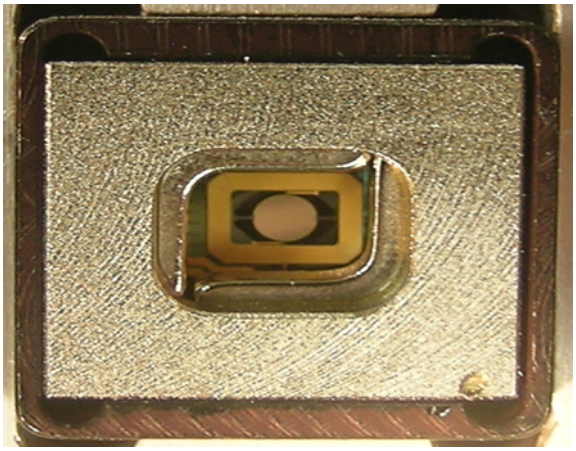


Figure 3.1: Microvision MEMS scan mirror provides two-dimensional rastering. Dimensions are 1.4 x 1 mm.

due to the necessary beam expansion ratio. The desire for a large area preview image affects the overall size and layout of the microscope which, as mentioned previously, needs to be as small as possible to facilitate *in vivo* clinical use.

The MEMS scan mirror, provided by Microvision INC., has an elliptical shape with a minor diameter of just over 1 mm. An input fiber coupler with a lens focal length of 4.5 mm was chosen so the input beam is 1 mm and does not overfill the MEMS mirror. Figure 3.1 shows a photo of the MEMS mirror and housing. A magnetic housing surrounds the mirror and is used for the actuation scheme. This magnetic housing protrudes from the plane of the MEMS mirror and limits the reflection angle of the laser beam, the repercussions of which will be considered in the next section. The mirror is mounted on two sets of hinges, one of which pivots about the minor axis and the other around major axis. A rectangular scan pattern is produced which consists of a fast scan direction and a slow scan direction. The fast scan runs in a resonant mode at a frequency of 22 kHz. Because of its resonant nature, the fast scan mirror displacement has a sinusoidal shape in time, producing an image that appears stretched at the edges, which must be corrected in software. The correction method

Table 3.1: Properties for the two microscope objective lenses used in the CIRSM design

Manufacturer	Mag.	NA	f	WD	XP diam.r	Parfocal Dist.
Nikon	50x	.55	4 mm	8.7 mm	4.4 mm	45 mm
Leica	100x	.75	2 mm	4.7 mm	3 mm	45 mm

is described in the next chapter. The slow scan of the mirror is linear at a rate of 60 Hz, producing a 60 Hz frame rate for imaging. The retrace time on the slow scan is much quicker than the forward time, so it can be assumed that the image takes most of the period.

The next constraint for the choice of telescope lenses was the rear aperture diameter of the objective lenses chosen. Because of the desire for variable NA from 0.55 to greater than 1.0, two microscope objective lenses were chosen which, when combined with the possible hemispherical front lens, provide for possible NA values of 0.55 to 1.1. The original method for providing a large area live preview of the sample was to allow for an imaging path in front of the objective lens. For this reason, and to accommodate the thickness of the hemisphere front lens, long working distance objectives were necessary. The two lenses shown in table 3.1 are the longest working distance objectives available for their given numerical apertures.

Path

The optical path and basic components in the microscope were described briefly in the Instrument Overview chapter on page 10. A zig-zag optical path is used to minimize the microscope length. Upon entering the microscope, illumination light travels 11.4 cm to the MEMS mirror, passing through the Raman filter set on the way. After reflection off the MEMS mirror the light travels through the first telescope lens, off a fold mirror, and through the second telescope lens before reaching the shoulder

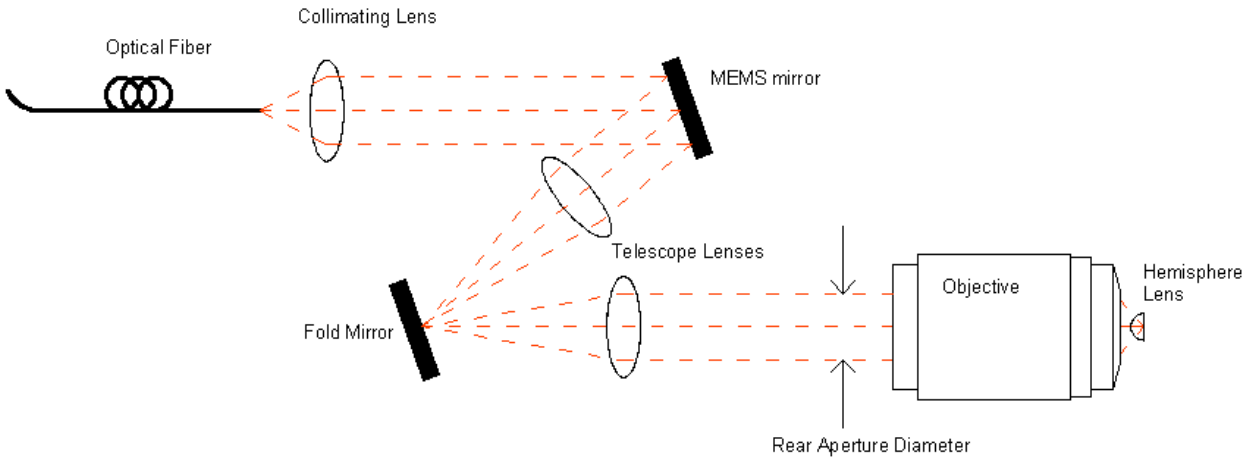
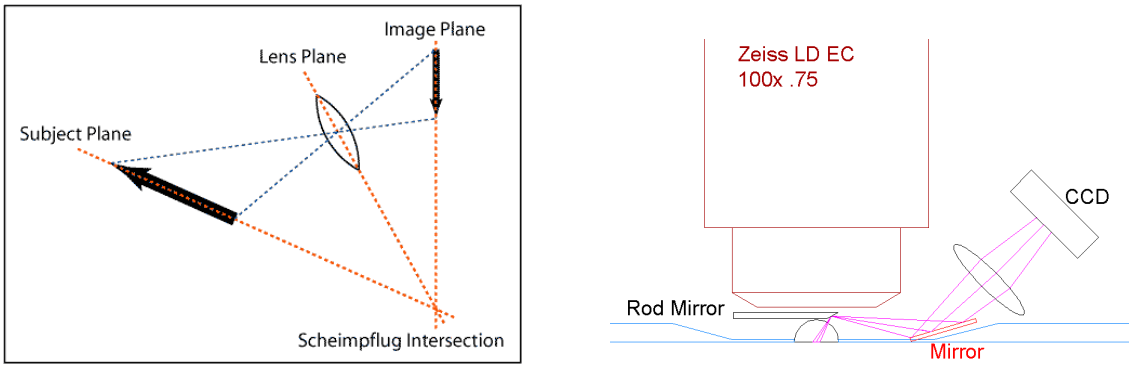


Figure 3.2: Block diagram of instrument subsystems. Curved red lines represent optical connections while straight blue lines represent electrical connections.

of the objective lens 26 cm later. This leaves room for an objective lens with 45 mm parfocal distance, as is the case for both of our objective lenses. An optional hemispherical lens can be placed with the vertex of the hemisphere at the focal point of the objective to increase magnification and NA. The diameter of the MEMS mirror limits the size of the illumination beam, and is the aperture stop in the system.

To ensure that magnification of the image remains constant when the focus of the object is changed, the system was designed to be telecentric. A telecentric system means that the chief ray is always parallel to the optical axis in the object space, and the exit pupil is located at infinity. Because it is physically impossible to place the scan mirror in the BFP of the objective lens, the telescope must image the mirror into the BFP to ensure telecentric imaging. This also aids in uniform illumination, as telecentric systems provide constant illumination and NA across the field of view [15].

Several methods were investigated for forming the large area preview image. The first idea was to place the CCD camera at a steep angle to the side of the sample and



(a) Scheimpflug imaging

(b) Miniature reflector

Figure 3.3: Attempted techniques for gathering a large area preview image.

use the Scheimpflug principle to form an image of the sample. Using this method, as seen in figure 3.3(a), an image can be formed when the object is at an angle with respect to the imaging lens and camera. If the plane of the object, lens, and camera all intersect at the same point, the entire image will be in focus at the camera. However, because the path lengths are different, the image has a keystone distortion, which could be corrected for in post processing. Upon investigation of this method, we found that we would have a maximum 27° angle with respect to the object plane to route the image out in front of the objective lens. This proved to be impossible because 30° or less with respect to the object plane is the total internal reflection angle limit for the interface between the BK7 hemisphere (index 1.5) and skin (index 1.3).

The second method investigated for relaying an image to the CCD was to use a small reflector to reflect the image to the side in front of the microscope. This method involved using a 45° mirror on the end of a 1 mm diameter rod placed between the front of the objective lens and the hemisphere, as seen in figure 3.3(b). This mirror would act like an aperture stop for the CCD imaging system, and relay lenses would be placed as close to the edge of the objective as possible to quickly image the light

onto the CCD. Due to the size of the camera, it would have been necessary to use a second mirror to route the light away from the front of the microscope and give adequate room for camera placement. It was found through Zemax models that using a 1 mm stop before any imaging lenses and more than 25 mm from the CCD could not produce good imaging results, so this method was also abandoned.

Having exhausted the available methods for gathering an image in front of the objective lens, we now opted to gather an image through the objective lens. This was done by placing a beam sampler directly behind the objective lens to reflect 5% of the light to the side, where an imaging system focused the light onto the CCD array. Gathering the CCD image behind the objective lens was a last resort because of the increased loss in the laser illumination and collection due to the beam sampler, and because it decreases the field of view for CCD imaging; however, it proved to be the only method that was feasible. To provide illumination for the CCD image a small white LED was placed so it illuminated the sample in front of the objective lens.

The sections that follow will detail the design and models used for the optical components, as well as specifications and justification for the choices of the components.

Lens Choices

In modeling the optical path, the first element in the design is the telescope, which expands the incoming beam and images the MEMS mirror into the back focal plane (BFP) of the objective lens. The fiber adapter used for the confocal channel contains a 4.5 mm aspheric lens and produces a collimated output beam diameter of 1 mm to fit the MEMS mirror diameter. In order to determine the necessary expansion ratio, the rear aperture diameter of our objective lenses must be considered. Part of the choice in objective lenses included comparing the rear aperture size so one set of telescope

lenses could be adequately used with both objectives. Since high NA is necessary for cellular structure discrimination, we assumed that we would primarily be using the 100x objective, so the beam expansion ratio of 3 was chosen to be optimized more for this objective. Because this expansion ratio does not completely fill the rear aperture of the 50x objective, there is a slight loss of NA from 0.55 when the lower power objective is used.

To aid in simplicity and reduce cost, it was desired to use off-the-shelf lenses for the telescope. Due to the need to minimize size of the microscope, and therefore optical path length, the first telescope lens was chosen to be the smallest possible lens available. Achromatic doublets were used for both telescope lenses because of their improved aberration performance over singlets. The parameters affecting the choice of the first lens were the scan angle produced by the MEMS mirror and the maximum reflection angle possible without vignetting the beam on the magnetic housing surrounding the MEMS. The maximum half angle of the scan was measured to be 14°. To properly image the MEMS into the BFP of the objective lens, the MEMS needs to be placed at the focal plane of the lens. Given these two parameters the maximum $f_{\#}$ of the first lens is found as:

$$f_{\#} \equiv \frac{f}{D} \leq \frac{1}{2\tan 14^{\circ}} \leq 2 \tag{3.1}$$

To keep the edge of the lens or lens housing from blocking the incoming beam, we tried to find a lens that was close to the $f_{\#}$ limit of 2. A 19 mm focal length half-inch diameter lens, $f_{\#} = 1.5$, was found to be the smallest available lens to fit this criterion. To give the desired beam expansion ratio of 3, the second lens was chosen to be a 60 mm one-inch achromat. These are both Thorlabs NIR achromats, models

AC127-019-B and AC254-060-B. This lens combination was modeled in Zemax to find the expected beam expansion and imaging performance, as discussed on page 32.

Given the maximum optical scan angle of 14°, the scan area at the sample can be calculated using the focal lengths of the objective lenses. These calculation yield a width of 326 μm for the 100x Leica objective and 653 μm for the 50x Nikon objective. With the addition of the hemisphere front lens, the area gets magnified by 1.52, the index of BK7 glass, to give a width of 217 μm and 435 μm respectively, which fits the field of view criteria set at the beginning of the chapter.

Typical microscope objective lenses are infinity corrected, meaning that when the sample is at the correct focus of the objective lens the ray bundles coming out the rear aperture are collimated. In a benchtop microscope a second lens, called a tube lens, is placed a distance behind the objective, and it is this lens that produces the first image of the sample. The eyepiece in a microscope then relays the first image and may add magnification. This infinity-corrected setup allows for the insertion of flat optical elements, such as polarizers, into the microscope for different analysis without introducing aberrations into the system. It also works nicely with our method of confocal imaging because the laser beam which is input into the BFP of the objective is collimated. However, the afocal nature of the objective lens output poses increased difficulty when trying to form an image onto a detector, such as a CCD.

Because the collimated angles out the back of the objective are diverging rapidly, we needed to place an aspheric lens as close as possible to the BFP to form this afocal space into an intermediate image. Then a second 1:1 imaging pair is used to relay this intermediate image onto the CCD. The aspheric lens is an 8mm Geltech lens, as this is the closest that a lens can be placed after the beam sampler reroutes the light from the objective lens. The 1:1 imaging setup is a matched pair of 19mm

achromats, as these are a short 1:1 relay solution with good performance. The model of this imaging system will be described in the next section.

Optical Performance

The imaging capabilities of the CIRSM can be described by two properties: the point spread function (PSF) and the axial response, also called the confocal response. The point spread function represents the response of the optical system to a point source object, and is useful for lateral characterization of the microscope. Because it is difficult to measure the point spread function, the edge response will be derived from the PSF calculation and used to compare with measured values. The axial response gives the cross-sectioning ability of the microscope, which is an important parameter for confocal microscopy because of the desire to reject out of focus light. For a more in-depth derivation of these parameters, Gu, Sheppard and Gan [16] as well as Dickensheets [17] can be referred to.

Point Spread Function

A diffraction-limited confocal microscope model is used for the derivation of the imaging capabilities. In this model, circular symmetry is assumed for all lenses and the optical fiber, so that $r^2 = x^2 + y^2$. For the ideal fiber confocal optical microscope, or FCOM, the detected intensity from the sample is

$$I = |p^2 * s|^2 \tag{3.2}$$

where $s = s(x, y)$ is the sample reflectivity and $p = p(x, y) = p(r)$ is the optical field in the sample plane and $*$ denotes convolution. For the assumed case where the sample is a point reflector then $s(x, y) = \delta(x, y)$ and $I = |p(r)|^4$, the point spread

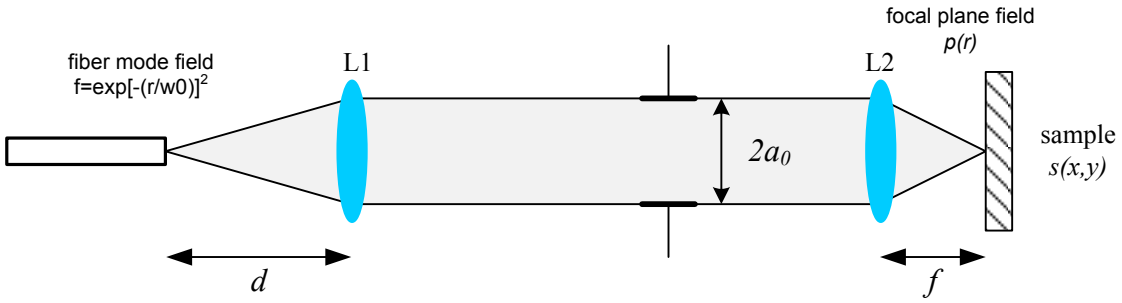


Figure 3.4: Simplified fiber confocal optical microscope (FCOM).

function of the FCOM. For a Gaussian beam input the PSF becomes [17]

$$I(r) = \left| \sqrt{I_0} \frac{2\pi w_0}{\lambda f w} \int_0^{a_0} e^{-(r'/w)^2} J_0(2\pi r r'/\lambda f) r' dr' \right|^4 \tag{3.3}$$

where a_0 is the pupil radius at the aperture stop, w is the Gaussian beam $1/e$ radius at the aperture stop, w_0 is the mode field radius at the fiber face, f is the focal length of the objective, r' is a dimensionless pupil variable ($0 < r' < 1$) and I_0 is the on-axis maximum intensity.

At this point, Gu and Sheppard use a dimensionless parameter, A, to simplify the transfer function by comparing the pupil radius to the Gaussian beam radius as

$$A = \frac{2\pi a_0 r_0}{\lambda d} = 2\left(\frac{a_0}{w}\right)^2 \tag{3.4}$$

where d is the focal length of the fiber collimating lens and r_0 is the is the intensity $1/e$ radius, $r_0 = w_0/\sqrt{2}$.

For the CIRSM the aperture stop is the MEMS scan mirror, and is considered to be circularly symmetric for with diameter of 1 mm to simplify calculations. Since this aperture stop is imaged by the telescope portion into the BFP of the objective lens, the objective lens exit pupil radius represents a virtual aperture stop (a_0) which is used in the calculations that follow. It is for this reason that the beam expansion is not modeled in the derivation above. Using the exit pupil diameter of the objective

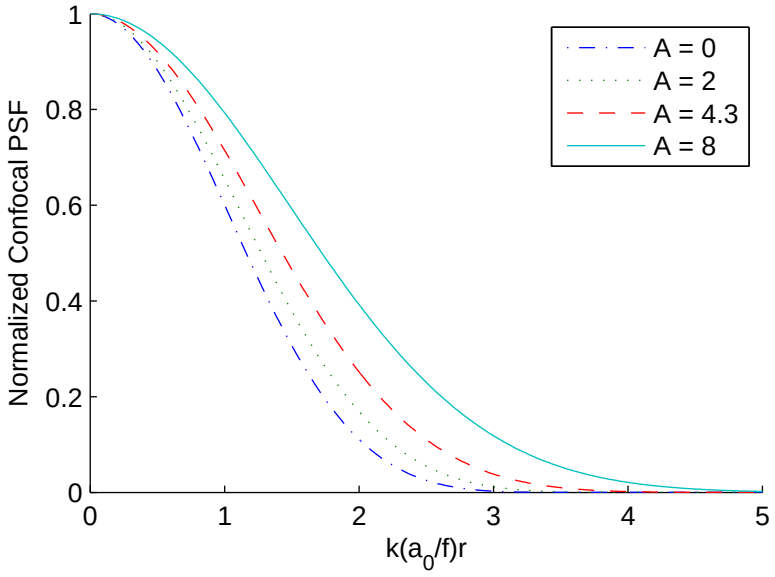


Figure 3.5: Normalized confocal point spread function profile for the ideal FCOM. The A=2 and A=4.3 curves correspond to the 100x and 50x objectives respectively.

lenses provides a good method for comparing the imaging performance of the two objective lenses when the same telescope is used, keeping the Gaussian beam diameter unchanged. A value of A=2 corresponds to the 1/e beam radius being equal to the aperture stop radius, as is the case for the 100x objective. An A=4.3 corresponds to the under filling of the aperture when the 50x objective is used.

Substituting the dimensionless A parameter into equation 3.3, a more useful form is found in equation 3.5.

$$I(r) = \left| \sqrt{I_0} \frac{1}{m} A \int_0^1 e^{-\frac{A}{2}p'^2} J_0(2\pi \frac{a_0}{f} r p') p' dp' \right|^4 \tag{3.5}$$

The quantity a_0/f represents the NA such that the Abbe sine condition is satisfied, whereby $\sin\theta = a_0/f$.

We can see from figure 3.5 that the fwhm of the PSF is 1.28 and 1.44 units for the 100x and 50x objective respectively. Calculating the units to obtain correct dimensions, this corresponds to fwhm values of 0.45 μm and 0.69 μm respectively.

The values for the edge response function, described in the following section, are of more importance for comparison with measured values.

Edge Response

The edge response of the system is an important parameter because it is easily measured. In practice the edge response function, or ERF, of an optical system can be measured by moving a sharp edge such as a razor blade through the focal plane of the system and looking at the intensity as a function of position. This yields nicely to confocal imaging because the illumination and detection paths are coincident, so any reflective surface with a clean edge can be used to measure the ERF.

Mathematically the ERF is the integral of the line spread function, the LSF, which is the integrated profile of the PSF.

$$LSF(x) = \int_{-\infty}^{+\infty} PSF\, dy \tag{3.6a}$$

$$ERF(x) = \int_{-\infty}^{x} LSF\, dx \tag{3.6b}$$

The edge response for a system is typically measured by the 10% to 90% rise distance. As shown in figure 3.6, the edge response distance is .49 μm for the 100x objective and .75 μm for the 50x objective.

Axial Response

The axial response of a confocal microscope is an important performance measurement as it corresponds to the cross-sectioning ability of the microscope. We used the V(z) response of a plane reflector moved through the focus of the microscope to quantify the axial response. Equation 3.7 on the next page gives the axial response of a fiber confocal microscope where $u = 2kz(1 - \cos\theta)$ is a defocus parameter with

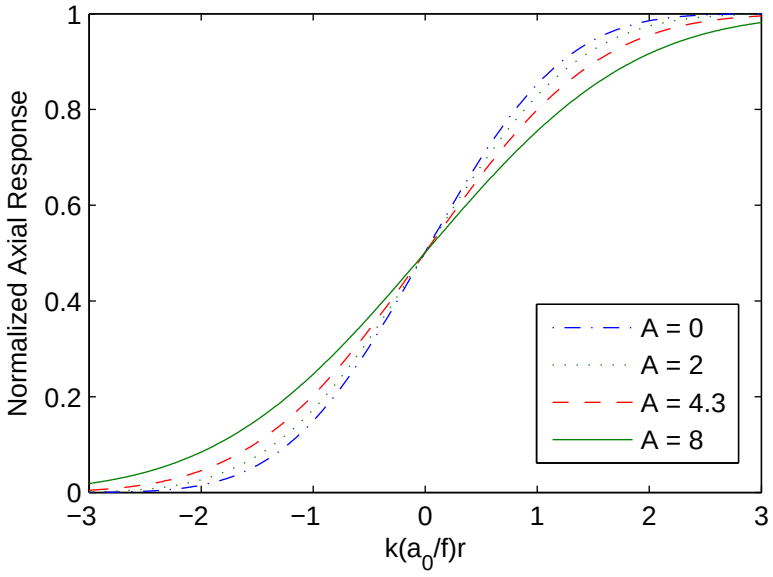


Figure 3.6: Normalized confocal edge response for the ideal FCOM. The A=2 and A=4.3 curves correspond to the 100x and 50x objectives respectively.

θ corresponding to the angle of the numerical aperture, NA= $n \sin\theta$ [16].

$$I(u) = \frac{A^2}{A^2 + u^2}(1 + e^{-2A} - 2e^{-A}\cos u) \tag{3.7}$$

Normalizing the response to its value for $u = 0$ gives:

$$\frac{I(u)}{I(0)} = \frac{A^2}{A^2 + u^2}\frac{(1 + e^{-2A} - 2e^{-A}\cos u)}{(1 + e^{-2A} - 2e^{-A})} \tag{3.8}$$

Figure 3.7 shows the theoretical axial response when using the 100x objective. Note the small difference in the FWHM value for A=0 and A=2. The A=2 value most closely represents the CIRSM with the 100x objective. The estimated FWHM value for the 100x objective is 1.2 μm. Because the beam diameter is not changed when using the 50x objective, the rear aperture is no longer filled, and an A value of 4.3 more accurately describes this situation. As seen in figure 3.8 this mismatch adds approximately .5 μm to the axial response FWHM, which is estimated to be 3.6 μm.

Because the design of this confocal microscope accommodates changes in NA from .55 to more than 1, figure 3.9 shows the variation of the theoretical axial response

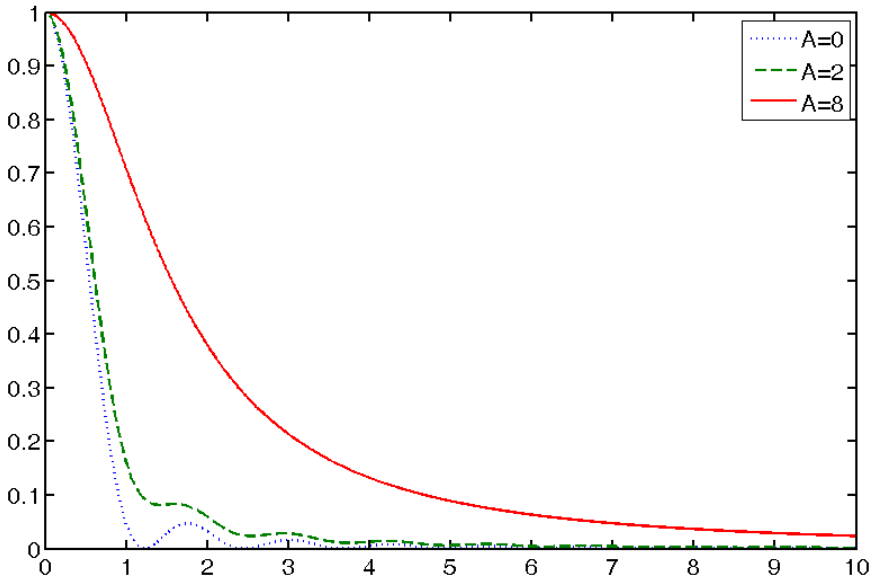


Figure 3.7: Axial response curves for different values of A with NA=.75. These correspond to Gaussian beam radius ω equal to ∞, a_0 (100x objective), and $a_0/2$.

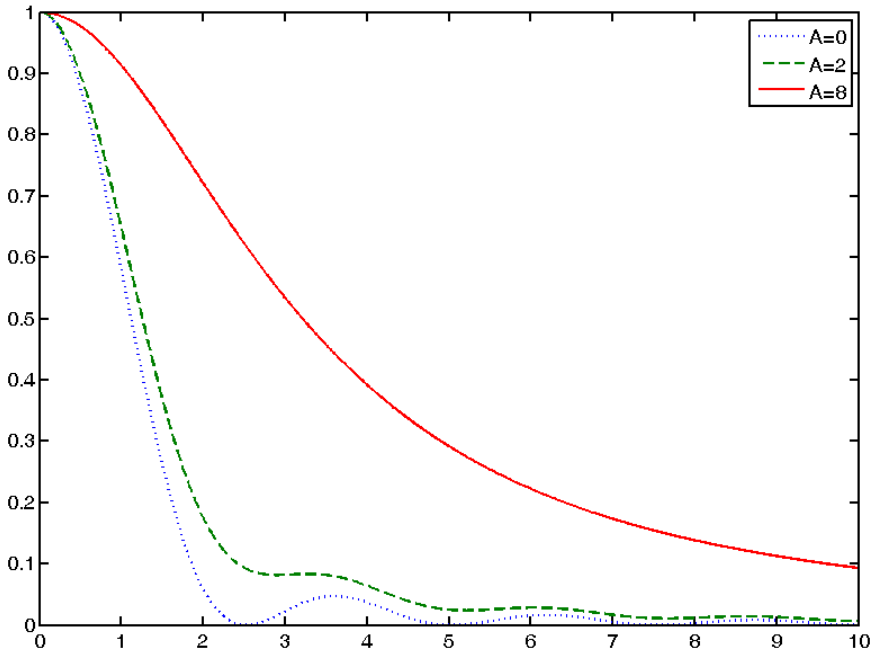


Figure 3.8: Axial response curves for different values of A with NA=.55. These correspond to Gaussian beam radius ω equal to ∞, a_0, $.68a_0$ (50x objective) and $a_0/2$.

fwhm. This plot assumes A=2, corresponding to a Gaussian beam radius equal to the pupil radius.

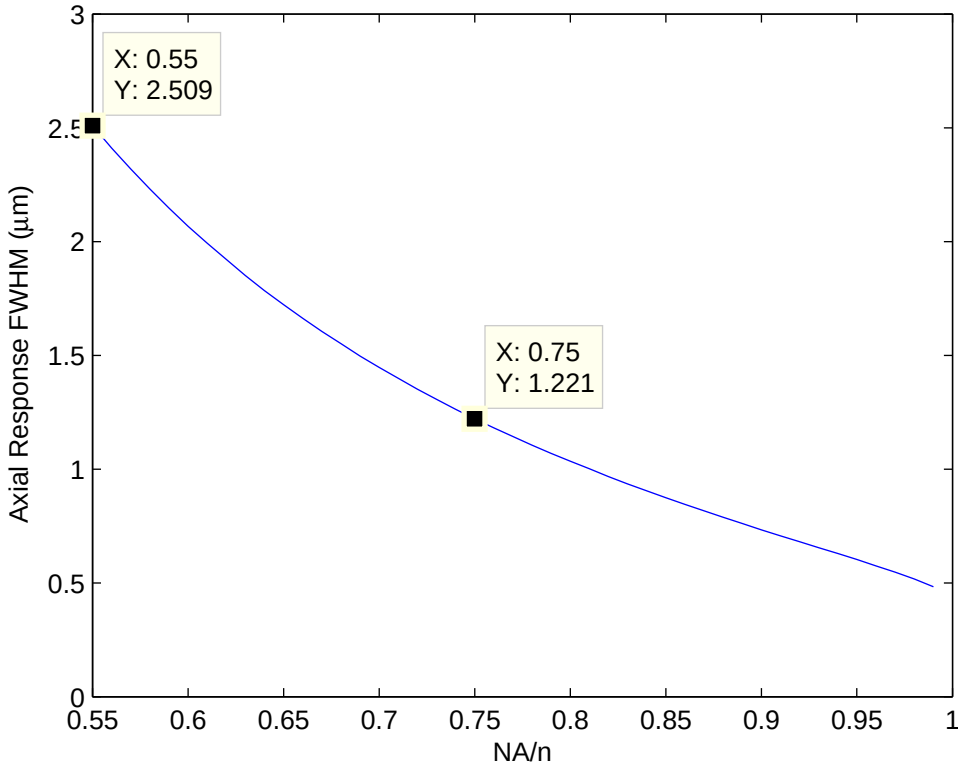


Figure 3.9: FWHM of the axial response as a function of NA. This plot assumes A=2, or that Gaussian beam radius equals the pupil radius.

Efficiency

Although the microscope resolution is best when the aperture is completely overfilled, or A=0, the amount of light lost due to clipping greatly reduces the return signal, which is critical for confocal imaging. The round trip efficiency can be modeled using the parameter A by setting $u = 0$ in equation 3.7 to produce [17]

$$\eta = \left|1 - e^{-A}\right|^2 \tag{3.9}$$

As seen in figure 3.10, overfilling the aperture of the objective lens greatly reduces the amount of light available for detection. When the Gaussian beam 1/e radius is matched to the aperture, the efficiency is about 75%. Past this point there is a trend of diminishing returns for increasing the value of A. This, combined with the near perfect edge and axial response for A=2, makes this the ideal compromise.

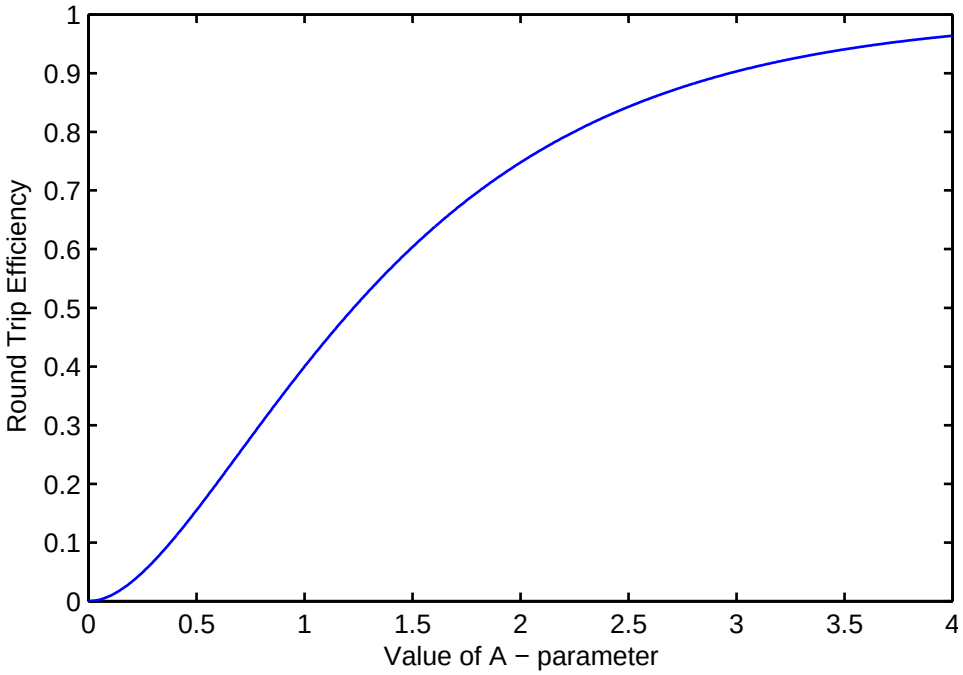


Figure 3.10: Round trip efficiency as a function of the dimensionless parameter A. At a value of A=2, corresponding to the aperture and 1/e beam radius being equal, the system is about 75% efficient.

Zemax Simulation

Zemax optical design software was used to verify the optical performance of the CIRSM. Because the objective lenses used in the microscope are commercial microscopy lenses, we assume they are diffraction limited and do not need simulation. The three parts of the microscope that were simulated in Zemax are the telescope, the hemisphere front lens and the imaging system for the large area CCD view.

Telescope

As discussed in the Lens Choices section, the lenses for the telescope portion of the microscope were chosen to minimize path length and therefore microscope size as well as provide adequate expansion to fill the rear aperture of the 100x objective lens. The positioning of these lenses is critical for both the beam expansion and imaging the MEMS mirror into the BFP of the objective, so Zemax was used to find optimal lens locations. Finding the optimal lens positions took three simulation steps. The resulting layout can be seen in Figure 3.11.

First, the spacing between the telescope lenses was optimized. During this step only the on-axis field was used, and the merit function was set to make the ray angle

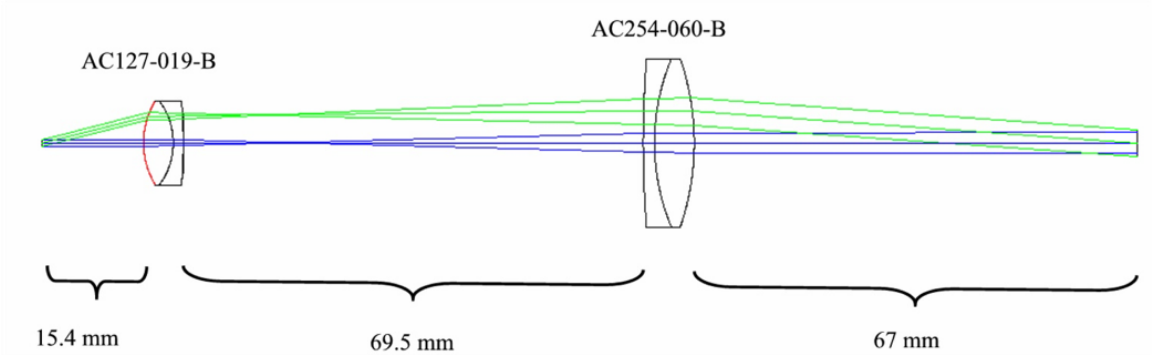


Figure 3.11: Zemax layout for telescope lens simulation

at the edge of the pupil past the second lens go to zero. This produced an output beam that was collimated well, and showed that the chosen lenses were expected to produce a beam with a diameter of 3.14 mm, realizing the design goal for a 3 mm beam diameter to fill the back aperture of the objective.

The next simulation step involved removing the on-axis field and replacing it with a 14° field. The merit function was then set to make the chief ray angle between the two lenses go to zero by varying the distance from the stop (MEMS mirror) to the first lens. At this point, both the telescope spacing and position of the first lens were optimized, but the off-axis field was much more distorted than the on-axis field.

The final simulation step was to include both the off- and on-axis fields and optimize for minimum wavefront error at the location of the BFP of the objective lens by fine tuning the telescope spacing. Since the 14° field is the extreme of the scan range, 5° and 10° fields were added to help with optimization of the entire field of view. The surface representing the rear aperture of the objective was set to be a circular aperture with diameter of 3 mm. Placing more weight on the results from the smaller angles produced good results close to the axis with larger wavefront error on the edges. The spacing between the second lens and the objective aperture was adjusted manually so the chief ray from the 0°, 5°, and 10° fields crossed at that point. The 14° field does not quite cross at the same point and is vignetted slightly. This optimization produced the optical difference fans seen in figure 3.12. The smaller-angle fields are around 0.1λ, and the larger fields are under 0.5λ, indicating reasonable performance. The lens spacings found during the telescope simulation were used during the mechanical layout to ensure correct positioning.

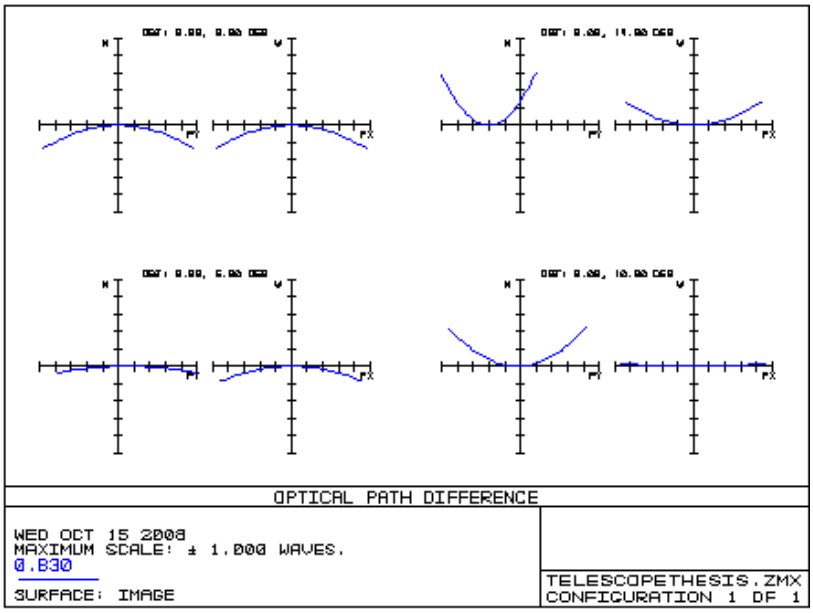


Figure 3.12: Optical difference for 4 field angles in the telescope simulation. Small angles produce good results while extremes are more distorted.

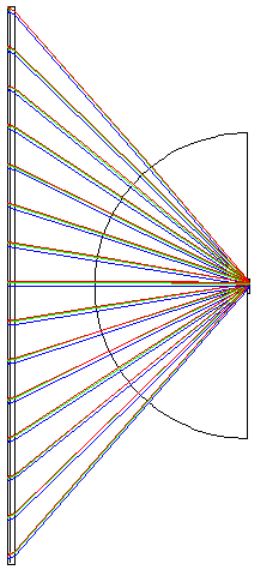


Figure 3.13: Zemax layout for modeling hemispherical front lens to increase NA. A thin flat piece of glass can be placed before the hemisphere to reduce aberrations when imaging at depth into skin.

Hemisphere front lens

The hemisphere front lens is an important part of the microscope design because it increases the numerical aperture of the objective lens and improves resolution of cellular structure. With the hemisphere placed so the vertex was perfectly at the focus of the illumination light, there are no additional aberration induced because the spherical wavefronts from the 0.75 NA input beam match the spherical surface of the hemisphere lens. However, simulations were necessary to understand the imaging characteristics as the illumination focal point was moved off axis as well as into the skin. For these simulations, a perfect illumination beam with NA=0.75 was used, as seen in figure 3.13. One of our goals was to find the off-axis image distance corresponding to a Strehl ratio of 0.8, which was assumed to be an indication of good imaging. The performance measures used to analyze the design were the spot diagram and optical difference (OPD) fans.

With the focal plane at the surface of the hemisphere the illumination beam was able to move up to 60 μm off axis before dropping below Strehl of 0.8. Figure 3.14 shows the spot diagram for this case, with fields at 0, 60 and 100 μm displacement. Knowing that our scan angle of 14° produces just over a 100 μm viewing radius, the outer field shows that even at the edge of our image we still have decent performance with a spot size just larger than the diffraction limit.

Imaging at depth into skin, which is modeled in Zemax as seawater, produces much more aberrated results. Performance was modeled at a depth of 50 μm, and RMS spot sizes of around 4 μm with optical difference fans showing almost 2 waves of aberration for the edge of the image (Figure 3.15(a)) were shown. Noticing that this result was primarily due to almost 7 waves of spherical aberration, we then used a thin piece of glass placed before the hemisphere lens to add negative spherical aberration

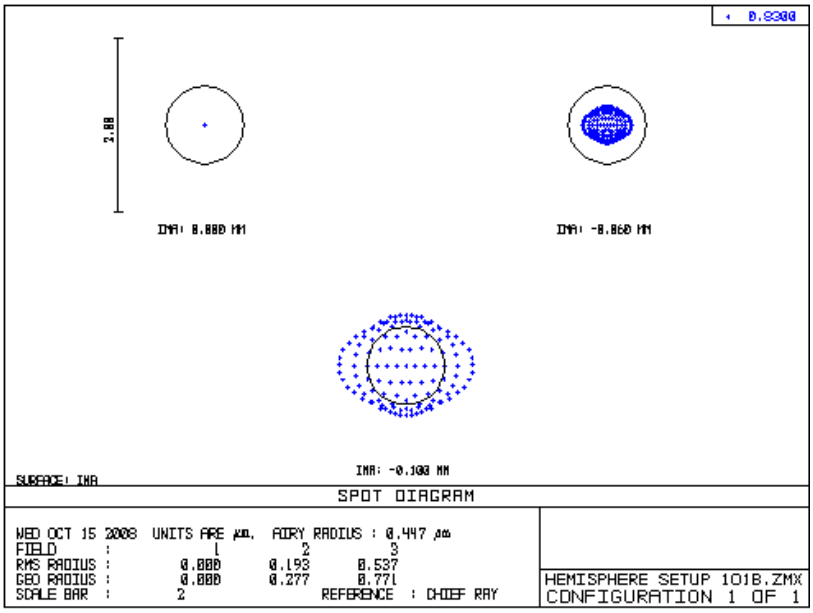
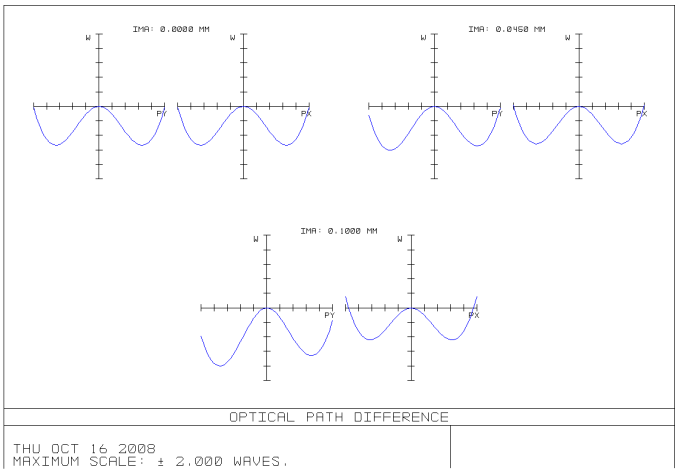


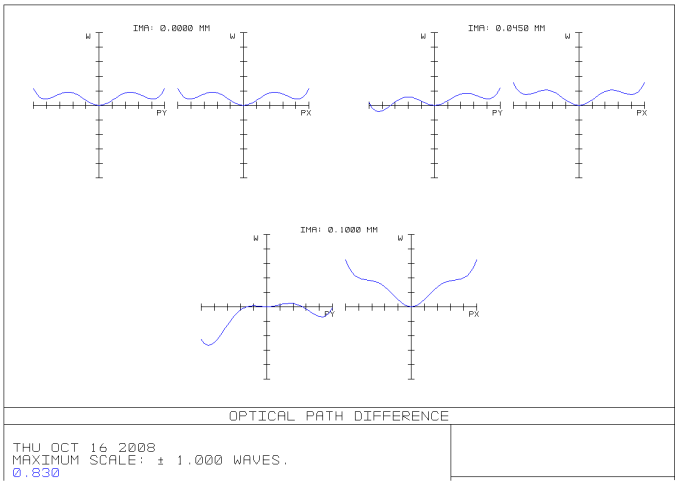
Figure 3.14: Spot diagram for fields at the surface of the hemisphere lens. The 60μm off-axis field corresponds to a Strehl ratio of .8.

and correct for the aberration induced by the hemisphere. This produced favorable results, producing OPD fans with less than 0.5λ aberration for most of the image area, as seen in Figure 3.15(b). This correction also showed RMS spot sizes of just over 1 μm, greatly improved over the uncorrected case. The thickness of the glass that produced the best results was found to be 135 μm, which is near the standard #1 coverglass thickness of 150 μm. When the standard coverglass thickness was used to model the performance, the difference in OPD fan and spot size were negligible. When imaging at depth using this technique with the coverglass, an off axis radius of 45 μm can achieved before the Strehl ratio drops below the desired .8 value. This method would be implemented into the design by placing a coverglass between the front of the objective and the hemisphere to optimize the performance for a desired depth, for instance 50 μm. Imaging performance would then be somewhat degraded

at the surface as well as further into the sample, but the depth of interest would have optimal performance.



(a)



(b)

Figure 3.15: OPD fans at 50 μm depth for the uncorrected (a) and corrected (b) cases.

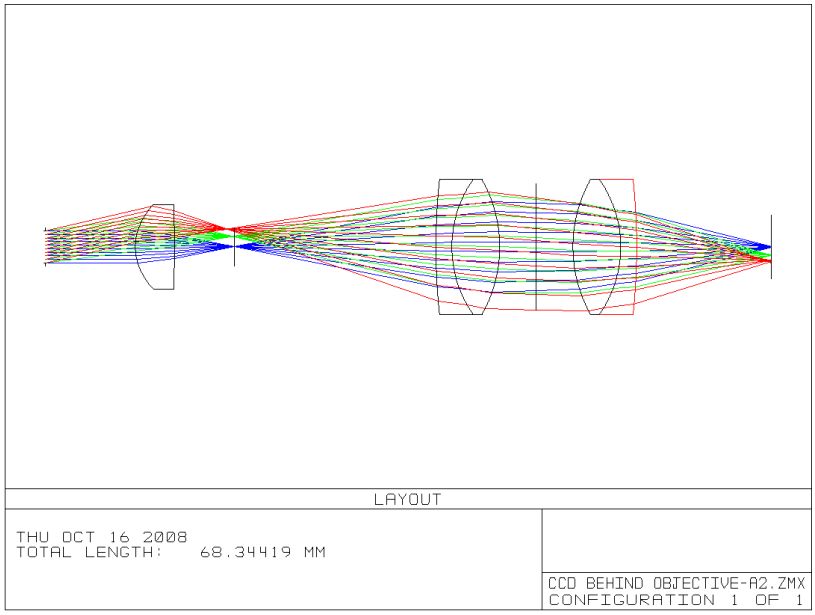


Figure 3.16: Imaging setup used to relay a large area image from the objective lens to a CCD board camera.

CCD Imaging Setup

Because of size restrictions, it was desired to place the CCD camera as close to the objective lens as possible. The first task was to redirect the reflected light, which was accomplished with a half-inch beam sampler placed just behind the rear aperture of the objective to redirect 5% of the reflected light from the sample to the side of the objective lens. Since large field of view at the object corresponds to large angles out of the back of the objective, a fast lens was need to produce an intermediate image. An aspheric lens was desired for this first imaging lens due to the good focusing properties of aspheric lenses when using collimated light. A Geltech 352240 asphere was chosen because of its short 8mm focal length and high NA of 0.5 to capture the maximum angular spread from the objective lens. Relaying of this image to the CCD, which is unable to be close enough to the objective to use the intermediate image because of

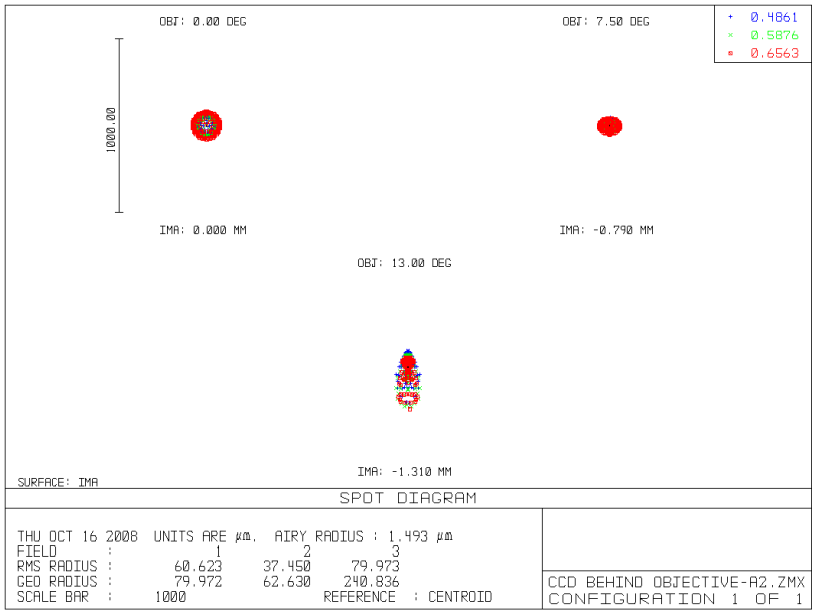


Figure 3.17: Spot size of the imaging system used for large area sample viewing.

the objective lens diameter, is done with a matched 19 mm achromatic pair, as seen in figure 3.16.

Figure 3.16 shows that the maximum collectible angle from the objective lens does not fill the 1/4 inch CCD sensor as desired. The magnification could be increased by moving the relay lenses closer to the intermediate image plane and refocusing the CCD, but the minimum spot size increases as well with this method. So whether the magnification was increased or a digital zoom implemented the equivalent minimum spot size remained nearly the same. Because of our desire for compactness, we chose to use the setup shown which does not utilize the entire CCD array as the increased magnification setup requires more path length. The spot sizes shown of 40 μm to 70 μm are 2-3 times the assumed color pixel size on the CCD camera of 20 μm. As can be seen in Figure 3.16 there is a visible amount of field curvature at the intermediate image plane which produces about 1mm of defocus at the CCD image plane for the

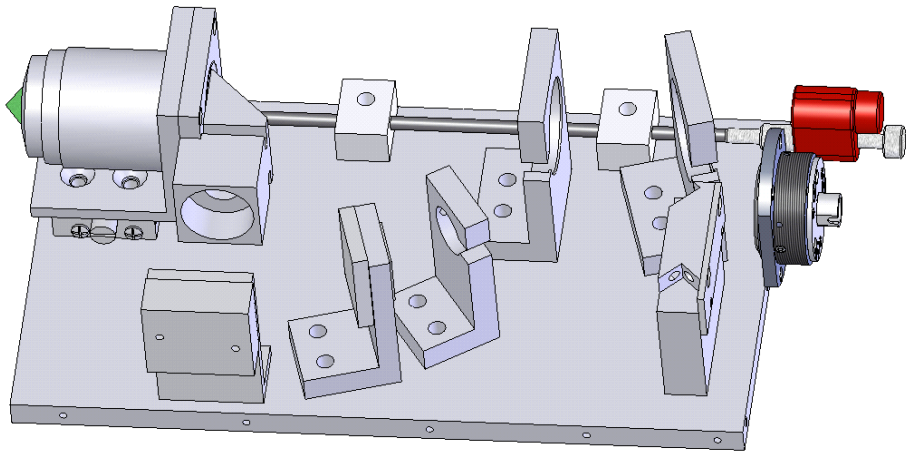


Figure 3.18: Rendering of microscope done in Solidworks.

outer part of the pupil. The effect of this can be seen in the sample CCD images on page 64.

Opto-mechanical Considerations

With the lens choices and spacings defined the mechanical layout for the CIRSM could be done. Solidworks was used to design the microscope, including the design of the individual parts as well as the overall assembly. The three-dimensional capabilities of Solidworks aided in visualizing the finished product and optimizing the design. A rendering of the design can be seen in Figure 3.18. Nearly all of the microscope components were custom parts including the lens holders, MEMS mirror holder, filter block, objective lens mount, and microscope housing. The most important considerations in the mechanical design were the focus control method and the adjustment degrees of freedom for alignment of the optical components.

Focus Control

Two methods of focus control could have been implemented in the CIRSM design. The first would be to translate the front of the microscope with the optical elements fixed. This method provides the best imaging because none of the optical elements move, and so can be precisely aligned and left in their optimal position. But, as the reader can imagine, trying to move the front plate of the microscope while holding it against a skin sample would be difficult and could produce problems with mechanical failure if too much pressure were exerted on the front plate. The only other option for focus control while keeping all of the optical components fixed would be to have all the components on a translation stage inside the microscope housing and move them all together. This is not possible, as such a solution would add tremendous mass and complexity to the design.

Instead, focus control was achieved by moving just the objective lens. This effectively changes the distance from the front of the objective lens to the sample and moves the focal plane. The only downside is that the position of the light entering the rear aperture of the objective lens moves as well, and might move away from the optimal location where the chief rays of all the scanned angles cross. Since the objective lens is only translated up to 200 μm, it was decided that a minimal effect on the location of the rear aperture would be induced. In fact, this translation distance is within the tolerance that the optics can be aligned by hand within the microscope anyway, and so does not pose any significant problems.

The method for moving the objective lens involved placing it on a translation stage and using a linear actuator to move the stage. A small one-dimension translation stage was found with a travel range of 5 mm, plenty of room for the required 200 μm focus control. Since we wanted the ability for computer controlled focus as well as manual

control, a New Focus Picomotor was chosen as the linear actuator. This actuator has a fine threaded screw which can be adjusted by hand or moved electronically by piezoelectric components within the device. To allow access to the adjustment screw the actuator was mounted on the rear plate of the microscope and a stainless steel rod used to connect the actuator tip with the translation stage on which the objective is mounted, as seen in Figure 3.18. Two Teflon supports were used to hold the steel rod in place and allow low friction movement.

Adjustment Methods

The lens and mirror holders in the CIRSM were designed to utilize a constant beam height above the baseplate. The fiber adapter used to launch light into the microscope has six degrees of freedom allowing for translation in x and y, tip, tilt, focus and rotation of the fiber. Using these adjustments the beam was first collimated then the angle of the exiting light moved until the beam was parallel to the baseplate. This ensures that he beam will pass through the center of the optical elements throughout the microscope. To aid in adjustment a second front plate was made with a 2mm hole in the same x and y location as the center of the fiber adapter, allowing alignment by moving the beam until it passed through this hole. Once the input beam was correct, further adjustment for proper collimation and lateral centering in the optical elements was done by moving the lens and mirror holders.

The mounting holes in the lens and mirror holders were designed to be large enough to accommodate small adjustments necessary to align the beam. The MEMS mirror mount and the fold mirror mount were rotated to make the beam pass through the center of the objective lens mount and the center of the hole in the front plate which the objective images through. The holders were moved laterally without the lenses present to center the beam in the lens holes, then lenses were inserted and the

holders moved axially to produce a well collimated beam past the second telescope lens. This adjustment method is not completely ideal because the axial and lateral movements are not decoupled, but providing decoupled adjustment methods would have increased the complexity and weight of the microscope significantly.

The removable front piece of the design has no adjustment since it attaches firmly to the front plate. The front piece is machined from magnetic stainless steel and held against three steel balls on the front of the microscope by magnets which are also in the front of the microscope. This design allows for the attachment of the front piece on the desired skin location using two-sided tape before the microscope is attached, as well as for the use of different front pieces which have either an aperture or hemisphere lens. Since alignment of the objective lens is critical to imaging performance when using the hemisphere lens, the holder which the objective lens is threaded into can be adjusted a small amount in the x and y directions to center it on the hemisphere. With the beam properly adjusted it will then fill the back of the objective lens and pass through the center of the hemisphere lens when the MEMS mirror is at rest. Since the adjustments on the objective mount to center it on the hemisphere were small, on the order of .001", the mounting screws were loosened until the plate holding the objective could just be moved by tapping it with a small screwdriver. By running the video and moving the objective lens back until it focused on the first curved surface of the hemisphere, the alignment could be altered until the reflection from this first surface was in the center of the image, ensuring centration on the hemisphere. The attachment and alignment mechanism for the front pieces can be seen in Figure 3.19.

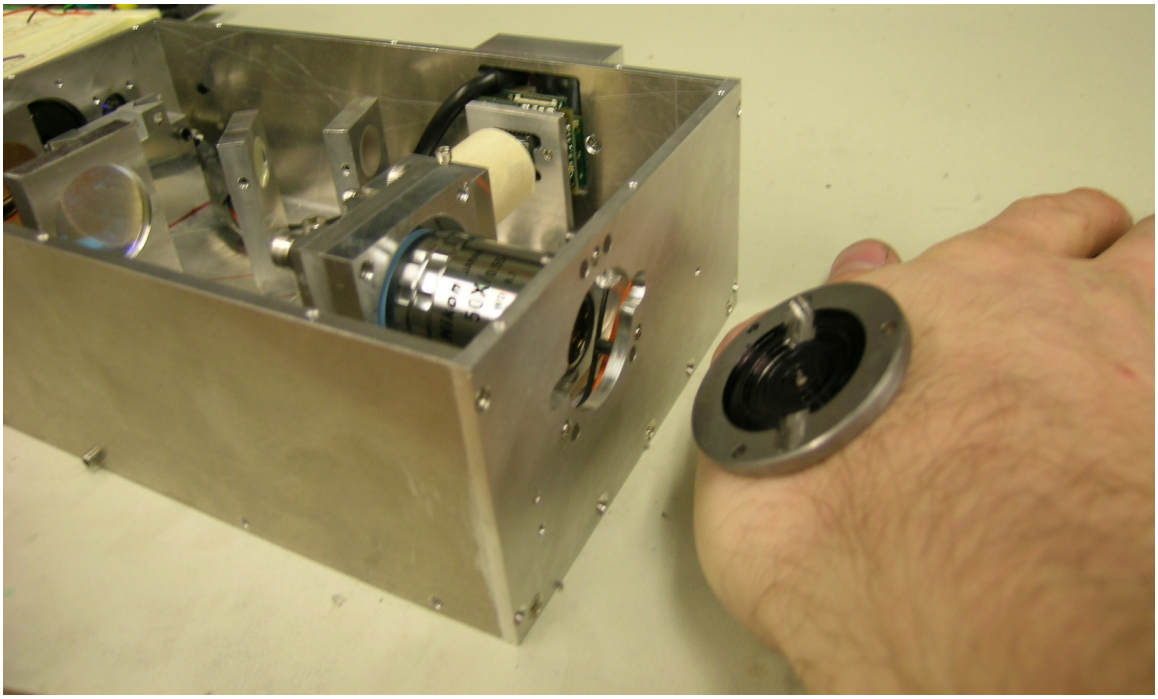


Figure 3.19: Stainless steel front pieces are centered using 3 steel balls and held in place by magnets on the front of the microscope.

ELECTRONIC DESIGN AND USER INTERFACE

Once the light reflected from the sample is incident on the APD used for detection, it enters the electrical domain. From here it must be amplified, conditioned, sampled, organized into an image, processed and saved. The amplification and conditioning was implemented on a PC board to interface between the APD, MEMS controller and image acquisition card. The first two sections of this chapter will describe the procedures for accomplishing this. The second two sections will detail the user interface and control features available from the computer workstation.

Amplifier Design

The image acquisition card used for sampling and image formation has four available ranges for full 10 bit sampling, .2, .4, .7, and 1.4 volts. Because these discreet voltage input levels do not allow for perfect matching of the APD voltage output an amplifier was needed to boost or attenuate the signal and match it to one of the available input levels. We also desired to add logarithmic compression capabilities to the amplifier to boost small signal gain, which may help in viewing intricacies in the cellular structure. The design includes three sections: the preamplifier, black level adjustment and logarithmic or linear amplification modes. Figure 4.1 shows the block diagram for the analog amplification scheme.

The preamplifier consists of a variable gain amplifier into which the signal from the APD is terminated. The variable gain amplifier is an Analog Devices AD603 and provides gain from -10 to 30 dB and bandwidth of 90 MHz. With the Hamamatsu C5460 APD, having a photoelectric sensitivity of 1.5×10^6 V/W and a minimum detection limit of 0.8 nW r.m.s, the minimum signal from the APD is 1.2 mV, for

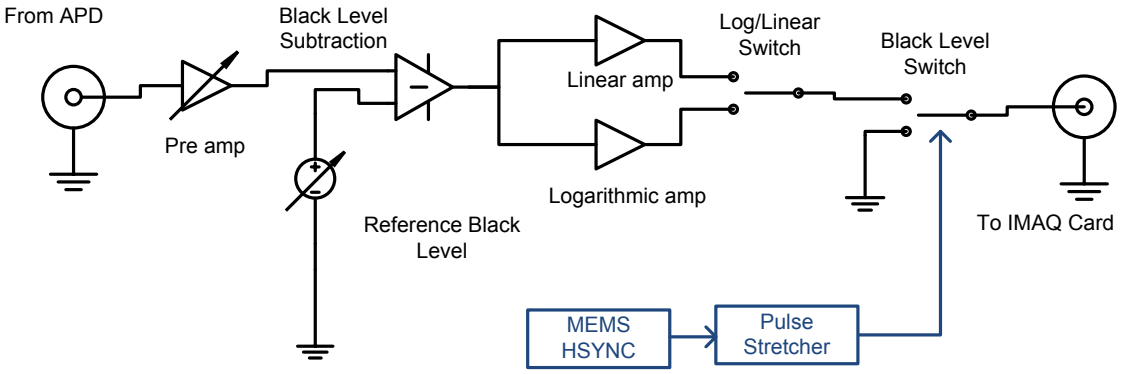


Figure 4.1: The amplifier design consists of a preamplifier, black level adjustment and logarithmic or linear amplification.

which the preamplifier gain of 30 dB provides adequate gain to match this voltage to the available full scale voltage levels on the IMAQ card.

The second section of the amplifier design is the black level adjustment. This adjustment is made by adding or subtracting a DC bias to the amplified video signal. When the IMAQ card reads the analog signal in and converts it to an image, ground is set as the black level in the video. So by DC offsetting the video signal with reference to ground we can adjust the black level in the image. This allows for fine tuning of the image and possible truncating of the noise by biasing the video signal so most of the noise is below the ground level and not acquired by the IMAQ card.

The signal is then fed to both a linear buffer amplifier and a logarithmic amplifier for the two available amplification modes. The logarithmic amplifier consists of an AD8310 log amp with an AD8138 front end to convert the input to a differential signal and add a bias so the log amp can function to DC. A CMOS switch provides for selection of either of the two channels to be connected to the output, which is 75 ohm terminated to match the video signal input termination on standard video input sources.

Image Formation

A National Instruments PCI-1410 was chosen as the image acquisition device because of its ability to acquire non-standard video. Because the signal from the APD and amplifier is not in a standard video format, like NTSC, the card needs to read trigger signals from the MEMS mirror controller to gather start of line and frame information. The signals available from the MEMS controller are a start of line, or HSYNC, and a start of frame, or VSYNC. The PCI-1410 has the ability to use these to trigger signals and generate an internal pixel clock used to digitize the analog video signal from the amplifier. The image size is set by two parameters - the number of lines in a frame, which is set by the MEMS controller, and the sampling frequency, which can is controlled on the IMAQ card. Since the HSYNC frequency is 22 kHz and the VSYNC frequency is 60 Hz we have about 360 lines available for an image. The number of pixels in a given line can be adjusted in the IMAQ control software, and are usually configured so the aspect ratio of the image is correct.

Image formation using the PCI-1410 takes place as follows. After the VSYNC signal is received, acquisition of the first line commences after the next HSYNC is received. Because the input to the card is AC coupled, a DC black level must be read during a specified clamping duration at the beginning of every line so the card knows how to DC restore the signal. This aspect is somewhat unfortunate and poses increased difficulty in the design of the amplifier as we must provide a black level at the beginning of every video line for the image to be formed correctly. After black level is set during the clamp portion of the video signal digitization begins. The user can define the number of pixels per line as well as the start pixel and dimensions of the actual image area. As mentioned previously, these parameters are typically adjusted

to give an accurate aspect ratio between the horizontal and vertical directions of the image.

To provide a black level for the IMAQ card to clamp to at the beginning of every line, the HSYNC pulse from the MEMS controller is also routed to the amplifier board. Because we need the ability to control the duration which the black level is provided in the video signal the HSYNC signal is first connected to a pulse stretcher, which provides for an on time adjustable from about 10 ns to several μs. This stretched HSYNC pulse is then used to change a second CMOS switch which has the video output connected to one input the other input grounded. This switch is located after the logarithmic or linear selection switch and is the last component before the output terminal. In this method the black level for each line is always set to ground and the apparent black level in the image is changed by adding or subtracting the DC bias described in the previous section to the video signal. Since the HSYNC pulse actually happens during the retrace time of the fast scan of the mirror, there is ample time after HSYNC and before the forward scan starts to provide this black level reference for the IMAQ card.

Due to the resonant nature of the fast scan produced by the MEMS scan mirror, the constant sampling, or pixel clock frequency, produced by the IMAQ card produces non-linear sampling of the image in one dimension, as seen in Figure 4.2. Since the velocity of the scan is slower at the edges of the illumination area more samples are taken in a given distance, causing the image to appear stretched on the edges. Since we cannot control the pixel clock this distortion must be corrected within software after the image is acquired. A simple processing technique was developed to accomplish this. The acquisition window is first set so the width corresponds to the maximum scan area and the turnaround point of the fast scan is just at the edge of the image. A MATLAB script was then written which reads the image and creates a sinusoidal

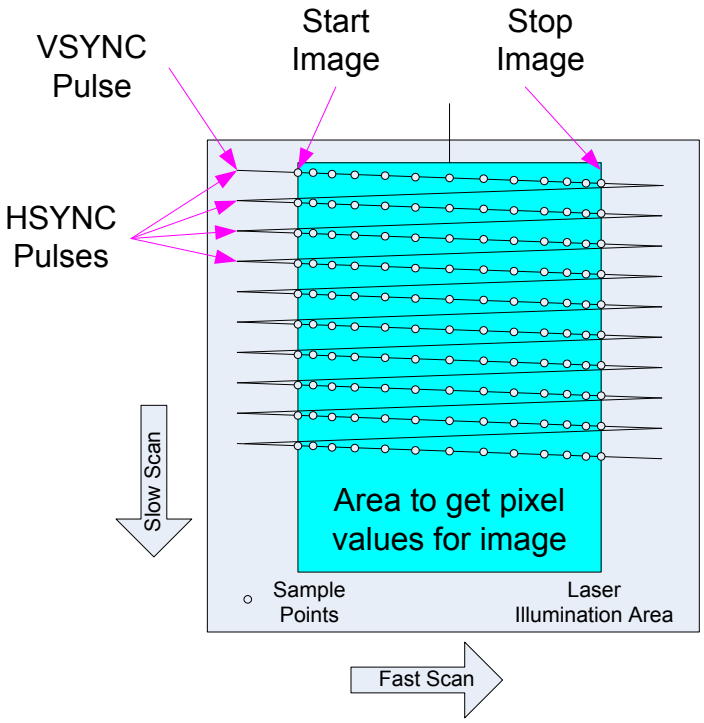
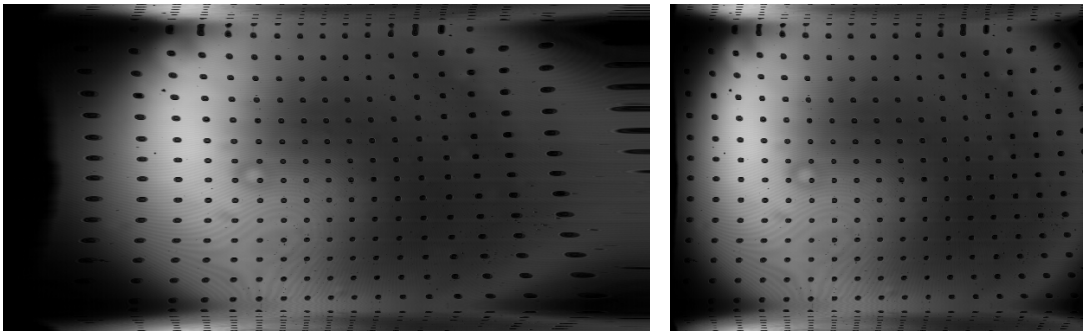


Figure 4.2: Sampling and image formation scheme. The MEMS fast scan is resonant and sinusiodal so more samples are gathered on the edges (slower scan speed at turnaround point).

representation of the number of pixels in the fast scan direction. By assuming that we want to keep every pixel in the center linear portion of the fast scan and taking out pixels on the edges to linearize the sinusoidal scan pattern a correctly dimensioned image is produced. The new image is reduced in dimension due to the discarding of pixels on the edges, as seen in Figure 4.3. This technique is easily implemented, but not as robust as an actual re-sampling of the image. Currently the images and video saved from the software do not correct the image stretching in real time, so all images and video must be post processed. Future developments will include real time correction as well as investigation into re-sampling techniques which may provide better quality.



(a) Initial image (b) After correction technique

Figure 4.3: The correction technique removes distortion due to the sinusoidal fast scan.

Focus Control

The Picomotor used to control the translation of the objective lens and provide focus control can be adjusted by hand or electronically. The electronic control is communicated via TCPIP to a network controller into which the motor is connected. The software interface was designed to provide the user with the ability to focus in and out, and define the incremental focus distance. Because the Picomotor is an open loop actuator, precise position control is not possible. Instead, the movement of the motor is calibrated and then assumed to stay constant. Calibration must be done using a micrometer stage, which limits the ability of general users to confirm correct calibration. During the calibration process a mirror is mounted on a z-translation stage and the focus of the objective lens found with the MEMS scanner turned off by reading the intensity of reflected light. After finding the focus, the motor is moved a set number of incremental steps and the translated distance measured with the stage and entered into the software, providing a forward focus constant. The motor then translates a set number of steps in the reverse direction and the user inputs the translated distance to provide a reverse focus constant. These numbers saved to

the computer and used to convert the desired incremental distance entered by the user into the GUI into the necessary number of steps to achieve the distance. While calibrating in this method provides a relatively accurate method of measurement, the actuation of the motor has been observed to change by small amounts from day to day, making maintaining a calibration beyond a few microns impossible. One future improvement in the CIRSM design would include using a closed loop actuator so no calibration scheme would be necessary and precise location known at all times.

User Interface

The user interface for the CIRSM was designed in the Labview environment. The software screen provides live video from both the confocal imaging and the CCD camera, with the ability to save images and video from both sources as shown in Figure 4.4. The CCD camera video can be turned on and off while the confocal image is running to increase computer resources if necessary. Control features incorporated into this software design include saving images and video, setting the black and white voltage levels on the IMAQ card, controlling focus position and frame averaging.

Due to noise which was visible during initial testing of the confocal imaging we realized the need to average video frames. This noise was visible as streaks or lines along the fast scan direction of the video, and because the streaks appear at random positions in the image, averaging several frames together provides a good way of removing the noise. Frame averaging is accomplished in a one in, one out fashion to preserve the natural frame rate. In this way the computer keeps track of a given number of previous frames and averages them with the current frame to produce the result, then the current frame is pushed down one position in the stack and the next frame is read in for averaging. Testing has shown that up to 10 frames of averaging

can be accomplished without degradation the 60 frames per second display rate. The user is able to turn averaging on and off as well as set the number of frames to average together while the image video is running. Averaging in this manner is effective at removing noise which is visible on the order of the line repetition rate, but is not helpful when trying to view quick movements such as blood flow. For imaging blood flow or other live events averaging must be turned off at the expense of increased noise.

Adjustment of acquisition parameters of the IMAQ card, such as the image area, start pixel, black level clamping location and sampling frequency, cannot be accomplished using the developed GUI. Since these parameters do not need to be adjusted beyond the initial setting, controls for them are not provided. To change these parameters the National Instruments Measurement and Automation Explorer must be opened and used to set the needed values, then changes are saved to a file. When the GUI opens this file is read and the necessary acquisition parameters loaded from it.

In Figure 4.4 the software interface can be seen in the background with live imaging running on the CIRSM. The image on the left of the computer screen is the live confocal image while the image on the right is the CCD camera view providing a larger area image. Shown here is an image of a hair on the subject's forearm.



Figure 4.4: Software provides a GUI for acquiring images and video and controlling focus, frame averaging, and gain.

RESULTS

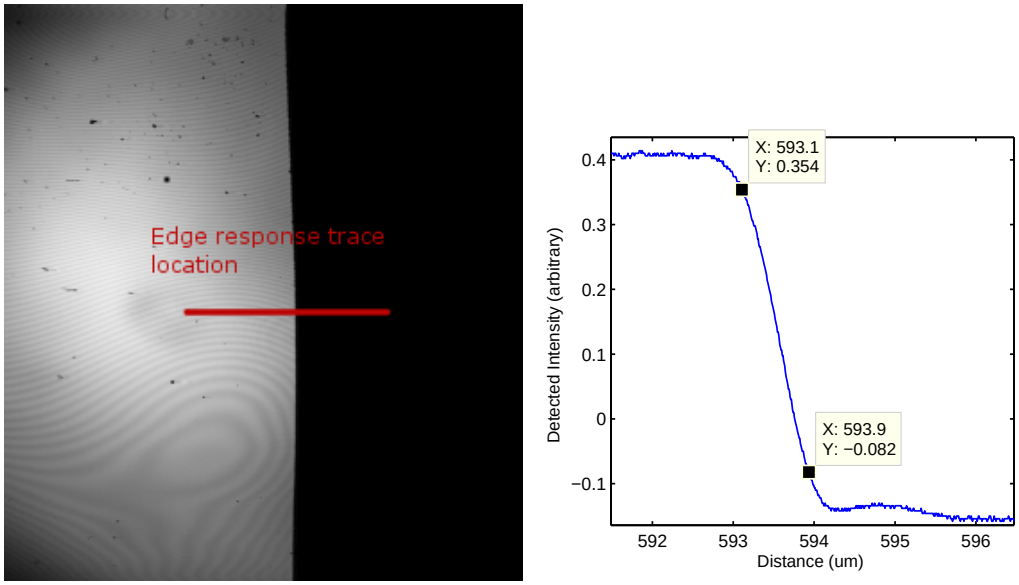
With the CIRSM assembled and functioning, the first task was to test the optical performance and compare with theoretical estimates. With performance characterized we then began testing the imaging and Raman sampling capabilities. This included imaging reference devices, such as other MEMS devices with known arrays of features, as well as many skin samples. Gathering image and spectra data from many different skin samples is an ongoing process, and the reason the CIRSM was built. Initial images and Raman results are presented in the second section.

Optical Performance

Edge response and axial response measurements were taken and used to define the optical performance of the confocal imaging channel and the Raman channel. These two measurements can be used to describe the volume which is integrated to provide intensity for a given pixel in a confocal image or a given spectra on the Raman channel. The edge response also deals directly with minimum resolvable feature size, which is more important for confocal image formation than the Raman channel response. The methods for acquiring the edge and axial response data for the two channels differed, so each will be discussed separately.

Edge Response

Edge response for the CIRSM was measured with a cleaved gold coated piece of silicon. This provided a good sharp edge with a highly reflective surface. The silicon piece was placed on a three-dimensional translation stage and moved until the edge was in the center if the image and oriented to be perpendicular to the fast scan. Because of the nature of the scan pattern produced by the MEMS mirror, the edge



(a) Image of edge

(b) Corrected oscilloscope trace

Figure 5.1: An image of the edge used (a) and the edge response(b).

response can only be gathered in the fast scan direction. This does not theoretically pose any difficulties because our design is circularly symmetric, so aberrations should have no dependence on rotation. With the edge placed in the center of the image area and at best focus, the output of the APD was connected to an oscilloscope and fall time traces were gathered for several different lines in the image. HSYNC and VSYNC signals were connected to the oscilloscope as well to provide triggers and enable acquisition of the edge data for any given line in the image.

Since the edge was placed in the center of the image, it was in the linear portion of the sinusoidal scan pattern so no correction was necessary to calculate edge response distance. Knowing the frequency of the fast scan and the maximum scan distance the maximum slope at this linear part can be calculated using

$$F(t) = \frac{A}{2} \sin 2\pi f t \tag{5.1}$$

$$slope = A\pi f \quad [\mu m/s] \tag{5.2}$$

Table 5.1: Edge response measurements for both objective lenses

	Confocal Channel	Raman Channel 50 μm fiber
50x Objective	.8 [.75] μm	N/A
100x Objective	.51 [.49] μm	2.1 μm
Note: [...] denotes theoretical value.		

where $F(t)$ is the sinusoidal fast scan in time and A is the width of one fast scan line. The slope, calculated with equation 5.2, is then used to convert the time scale from the oscilloscope traces to a distance scale for edge response evaluation. The width of the fast scan lines was measured by imaging another MEMS mirror with 30 μm via spacings and counting the number of vias as seen in Figure 4.3. This calibration method was verified by applying the calibrated distance axis to an oscilloscope trace showing two vias in the center of a fast scan line and confirming the distance between them was 30 μm. Table 5.1 shows the results from these measurements for both the 50x and 100x objective lenses.

Because we desired to use a Raman spectra to characterize the Raman channel, the edge response could not be obtained during image acquisition. Instead a cleaved silicon sample was mounted on a translation stage and adjusted axially to find the focal point, then translated laterally in small increments while obtaining a Raman spectra at each increment over the edge of the silicon. This method does not provide as much accuracy as the method for the confocal channel because we are now limited by the resolution of the micrometers attached to the translation stage - about 1 μm. Results for the Raman channel were collected using a 50 μm core fiber since this fiber was seen to provide the best compromise between collection efficiency and confocal rejection, which will be shown in the next section.

The edge response values in Table 5.1 compare well with the theoretical values of 0.49 μm and 0.75 μm for the 100x and 50x objective respectively, as given on page

27. The slight increase in edge distance over the theoretical values could be due to aberrations introduced by the telescope, misalignment of the optical components, or slight defocus in the position of the edge. The Raman channel edge response value for the 50x objective was not obtained because the 100x objective was used primarily in the skin measurements to provide greater magnification and cell detail.

Axial Response

The methods for measuring the axial response of the confocal and Raman channels differed as the Raman spectra had to be gathered at each depth position on the spectrometer. For the confocal channel a mirror was placed in front of the objective lens and the Picomotor used to translate the focus of the objective through the mirror while recording the reflected intensity using an oscilloscope. By gathering one scan, then moving the mirror 20 μm back and taking another scan the distance between the peaks of the two scans can be used as the control to calculate the distance in microns of the axial response, as seen in Figure 5.2. This method was necessary due to the scale from the oscilloscope being in time units. The axial response for the two objective lenses was measured both with and without the hemisphere front lens, the values of which can be seen in Table 5.2. Theoretical values for the confocal channel are given in the table for comparison. However, the theoretical development of the PSF and axial response assumed the illumination and detection fiber to be the same, so the response of the Raman channel using a larger fiber size has no theoretical comparison.

Measuring the axial response for the Raman channel involved using a polished silicon sample and taking Raman spectra at set intervals as the objective was moved through focus. A spectrum was obtained, then the Picomotor used to increment the focus position by 1 μm, then another spectrum obtained and so forth. In this way

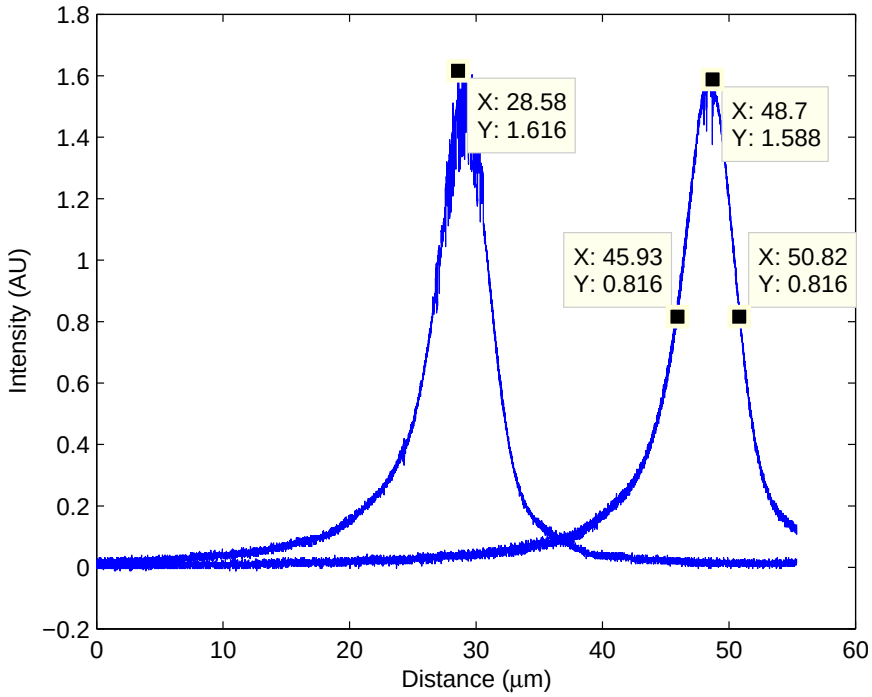


Figure 5.2: Moving the mirror 20 μm between axial scans allows for calculation of the distance axis and the FWHM axial response. This plot was taken with the 50x objective.

we measured an axial response with approximately 1 μm error due to the inaccuracy in the Picomotor movement. Results from these measurements can also be seen in Table 5.2.

As eluded to in the last chapter the collection efficiency of the Raman channel is highly important due to its direct relationship to necessary integration times. Taking Raman spectra from skin samples can take as long as one minute per integration. These long integration times produce errors in the spectra obtained due to more probable movement of the sample during the integration, so cutting this time is important. An investigation of the collection efficiency compared with axial rejection was done to find the optimal collection fiber size, since the collection fiber size directly relates to both the collection efficiency and confocal rejection. As Figure 5.3(a) shows the collection efficiency, shown as detected intensity, increases substantially from a

Table 5.2: Axial response measurements for both objective lenses

	Confocal Channel		Raman Channel 50 μm fiber	
	Air	Hemisphere	Air	Hemisphere
50x Objective	4.8 [3.6] μm	4.1 [2.8] μm	24 μm	17μm
100x Objective	2 [1.2] μm	1.5 [.92] μm	12 μm	9 μm
Note: [...] denotes theoretical value.				

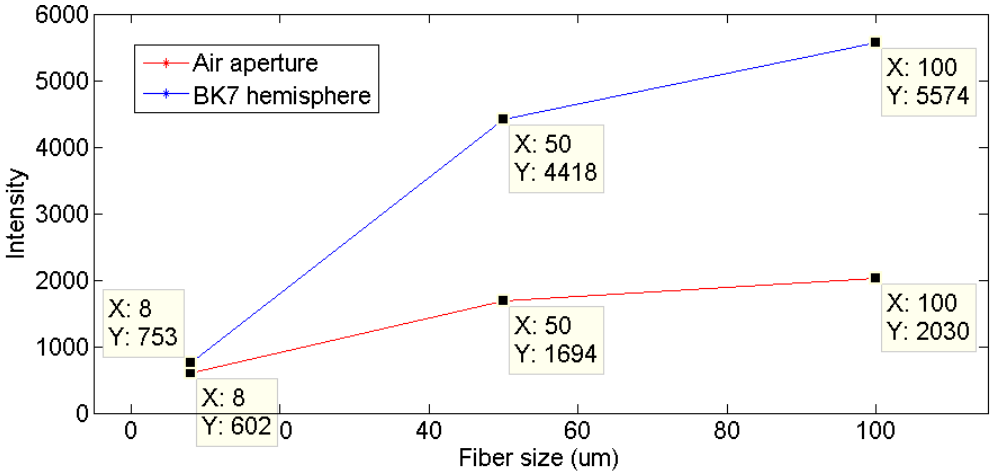
fiber with an 8 μm core to a 50 μm core, but much less on the next jump to a 100 μm core. These values were measured by looking at a Raman feature from the silicon sample using equal integration times for each fiber size. Figure 5.3(b) shows the increase in the FWHM axial response value as a function of fiber diameter. From this data set we concluded that the 50 μm core fiber provides a good compromise between collection efficiency and axial response, or confocal rejection, which is the justification for the use of the 50 μm core fiber in the other experiments.

Imaging

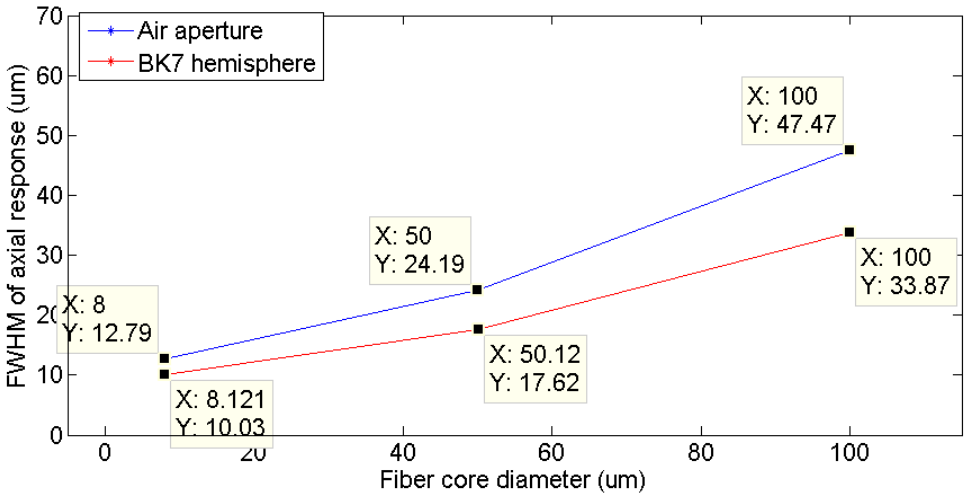
Confocal Imaging

The design of the CIRSM allowed for confocal imaging using two objective lenses to test performance with different magnifications and NA. However due to our desire to see cellular structure, the 100x objective has been used almost exclusively for skin imaging. Figure 5.4 provides an image taken with the 50x objective and showing the relative image area for the 100x objective. From this, the reader can see that while the 50x objective gives a larger overview of the skin surface, detail in the cell structure is not visible.

In testing the skin imaging capabilities of the CIRSM we noticed that the front piece with the aperture was difficult to use when holding the microscope by hand.



(a) Raman intensity vs. fiber size



(b) Raman axial FWHM vs. fiber size

Figure 5.3: Comparison of collection efficiency and axial response vs. fiber size.

Because the skin bulges through the aperture somewhat any minute changes in the pressure of the microscope against the skin would cause changes in focus. For this reason, the hemisphere front piece was used primarily for imaging. Because the skin is pressed firmly against its flat surface no changes in focus were seen when altering the pressure of the CIRSM against the skin. Using this setup, images and video of several skin types and locations were taken. Sample images of different locations and types of skin can be seen in Figure 5.5. The cross sectioning ability of the CIRSM allows for good imaging of cell membranes and nuclei in the fingertip as well as providing rejection of upper skin layers to allow viewing of the dermis-epidermis junction, as is evident in Figure 5.5 showing the melanin caps present on the dermal papillae, which is about 80 μm below the skin surface. As further evidence of penetration depth capillary loops were easily found with the confocal video showing blood cells flowing within the vessels. These capillary loops, which lie under the papillae, are usually between 100 and 120 μm below the surface of the skin, so the ability of the CIRSM to see them confirms the ability to penetrate to depth desired in the design. The capillary loops and blood flow are easily seen in the confocal video, but still images do not provide enough detail to make out the features, so no images of these features are shown.

The confocal images taken with the CIRSM are very promising, but also reveal some bandwidth problems in the detection scheme. Though not extremely evident, the bright spot in the images are somewhat stretched in the fast scan (vertical) direction. This stretching is most likely due to inadequate bandwidth of the APD. One future improvement to the imaging system is to use a faster detector and eliminate these stretching artifacts.

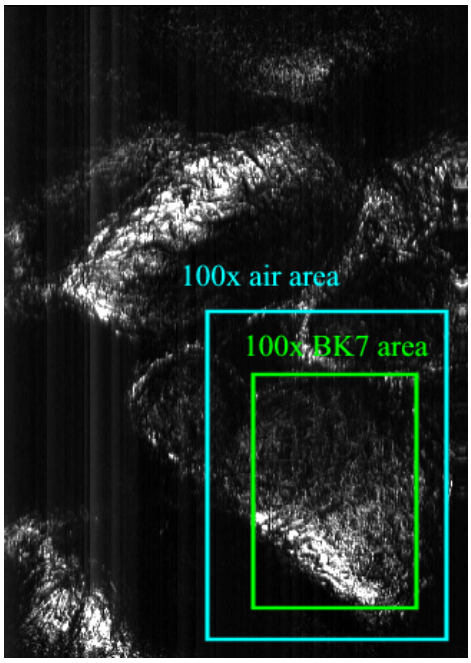


Figure 5.4: Skin image taken with the 50x objective. The boxes show the image areas for the 100x objective with and without the hemisphere. The increased magnification using the 100x provides more structural detail on the cellular level.

Large Area CCD

The CCD large area imaging designed for confocal guidance and alignment did not prove as useful as expected. Initial images taken with the 50x objective and the aperture front piece provided nice images and helped with guidance of the confocal imaging. However, when we moved to the 100x objective the decrease in working distance in front of the objective lens made getting the LED light to the sample much more difficult. The amount of white light present at the sample decreased enough to limit the CCD imaging when using the aperture front piece. With the hemisphere front piece CCD camera imaging with the 100x objective proved impossible. For the large area CCD imaging to be useful with the high magnification objective lens another method of sample illumination would be necessary. One possible alternative would be to use large diameter fibers which could be routed through the small

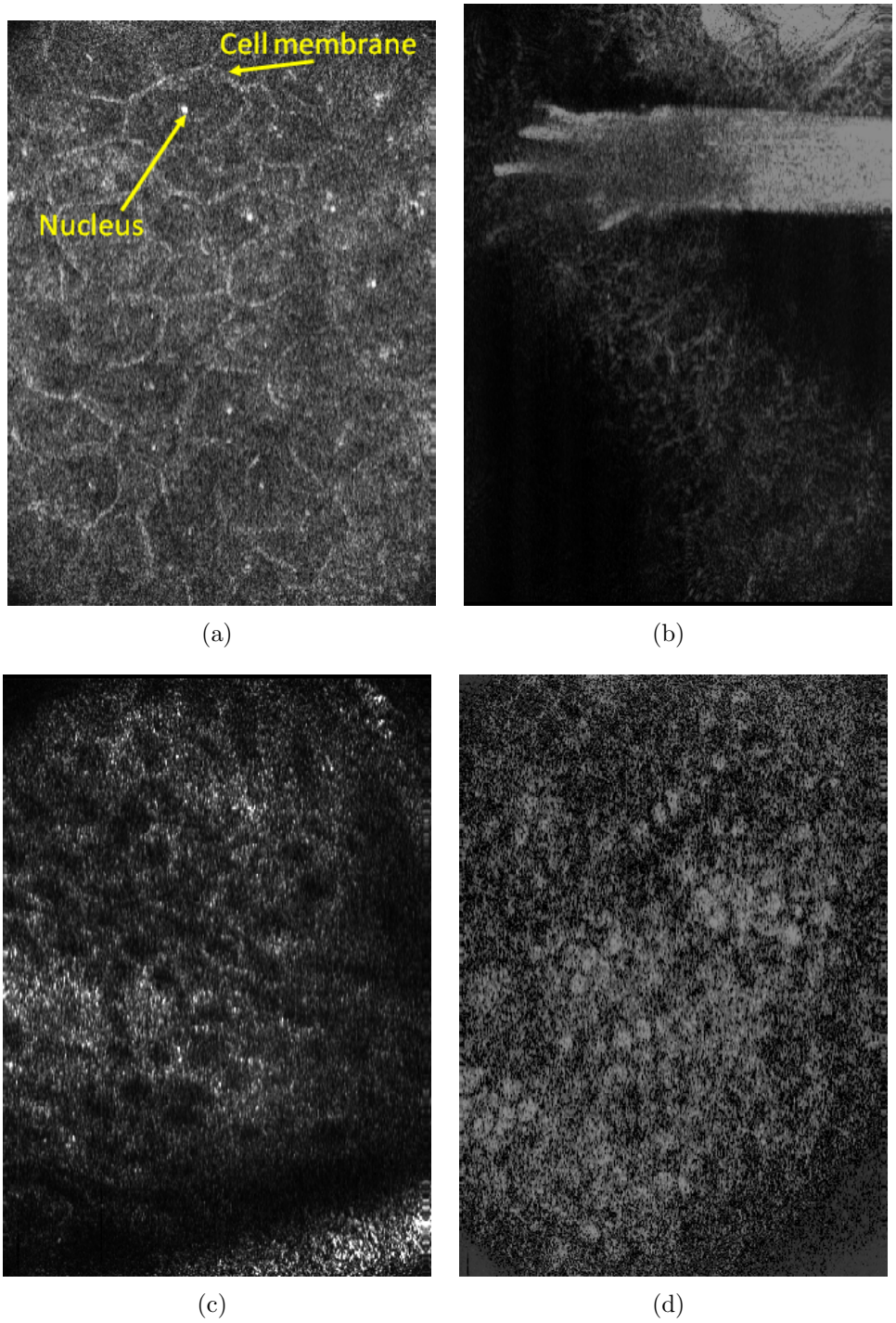
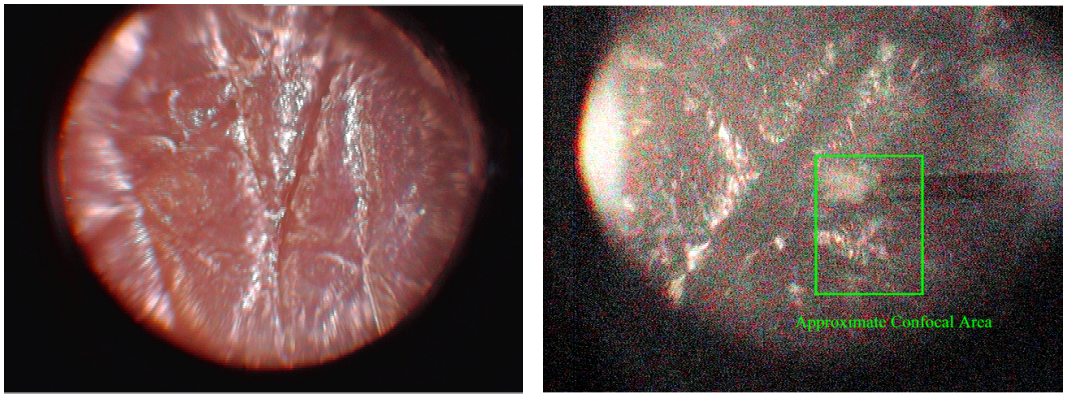


Figure 5.5: Confocal image of fingertip showing cell membranes and nuclei (a). The base of a hair and surrounding tissue is shown in (b). In (c) the dark round areas are cell nuclei within the dermis in the arm. Round white areas in (d) are the melanin "caps" over dermal papillae, which are more visible with darker skin types.



(a) 50x aperture (b) 100x aperture

Figure 5.6: Large area CCD imaging works well for the 50x objective (a), but not for the 100x objective (b) which corresponds to the confocal image in Figure 5.5(b). These images were taken using the aperture front piece. CCD imaging with the hemisphere did not produce viable results.

space between the front of the objective lens and the sample. Investigation of other illumination techniques such as this will be done in future work.

Raman Spectra

Initial Raman spectra of skin were obtained using the CIRSM configured with the 50x objective lens and hemisphere front piece. Because Raman scattering is such a weak process, especially in skin tissue, integration times of 30 seconds or longer were necessary to produce good spectra. Another important aspect of gathering Raman data is the laser intensity at the sample, with more intensity producing increased Raman scattering and decreasing integration times. The intensity limit for approval of clinical trials for the CIRSM was set at 40mW at the sample, so we tried to get as close as possible to this intensity. The spectra obtained in Figure 5.7 were taken with laser intensity of 38.5 mW at the sample and integration time of 30 seconds. These initial Raman spectra were taken before the confocal imaging was functioning,

so there are no correlated confocal images. Raman spectra, such as those in Figure 5.7, are typically area normalized to produce plots which can be analyzed for relative peak intensities.

With confocal imaging working well we set out to gather correlated confocal images and Raman spectra. However, because of the interference issues with the circulator setup, we cannot deliver enough power to the skin sample for Raman spectroscopy when operating in the low throughput mode of the circulator, which is necessary for good imaging. Because of this, simultaneous imaging and Raman spectra can not be gathered until a different method of light delivery and detection is developed to allow more power to be delivered to the sample. We were able to take confocal images, then rotate the polarization input into the circulator to deliver enough power to the sample to gather Raman spectra from skin within a period of approximately one hour, proving the concept of correlated confocal imaging and Raman spectroscopy is possible in the CIRSM. It is also important to note that the MEMS scanner must be turned off during Raman sampling as any movement in the sample location produces noise in the spectra. Since the movement can blur Raman spectra it is important for the microscope to be held still on the sample during acquisition, another reason for low integration times which reduce the chance of movement during acquisition.

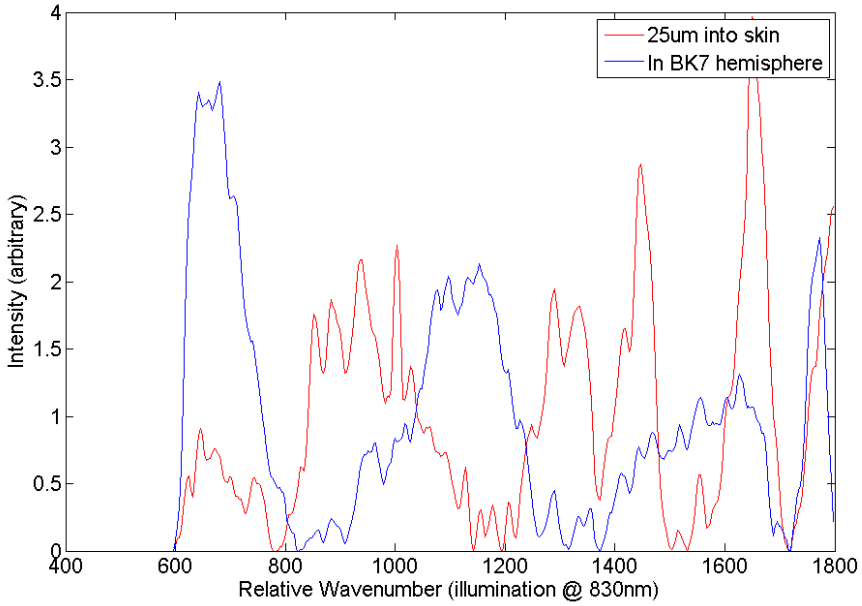


Figure 5.7: Raman spectrum of normal skin taken with the 50x objective and hemisphere. The spectrum with the laser focused in the BK7 hemisphere is given for a reference.

CONCLUSION

Skin cancer is one of the most common cancer types in America, with new cases affecting over one million Americans last year [1, 2]. As part of the diagnosis process, 5.5 million biopsies and histology are performed each year, over 70% of which turn out to be benign [18]. With the cost of biopsy and histology around $500, it is costing the US health care system $2 billion every year to detect normal skin. The microscope developed for this project incorporates two powerful cancer diagnostic tools, confocal microscopy and Raman spectroscopy, into a small hand held unit which can be used in a clinical setting. We hope the ability for gathering data *in vivo* will improve diagnosis time, provide greater patient comfort, and reduce the cost of unnecessary histology of benign lesions by decreasing the false positive visual diagnosis rate.

Optical testing of the microscope has shown its performance to be very close to theoretical values, realizing our goal of making a compact unit which performs near that of large bench top microscopes. The images and Raman spectra of skin have shown proof of concept for a combined confocal imaging and Raman spectroscopy microscope. Though simultaneous confocal images and Raman spectra have not yet been obtained, the feasibility of this has been shown, and short term future work on the laser illumination scheme will make this possible. Further development of small confocal and Raman microscopes will reduce cost over larger units and make standard clinical usage more feasible.

Future Work

The most important goal for future work in this project if further miniaturization of the microscope. Though the microscope that was developed can be held by hand

and used for *in vivo* skin imaging, its bulk and weight limit the ease and duration of use. Along with miniaturization is the goal of a more ergonomic design to allow the user an easier method for holding the microscope, as well as a smaller front end to accommodate better visual alignment with skin features. Other future goals include improved image resolution, which would require more control over the MEMS mirror, elimination of bandwidth artifacts by using a faster detector, real time image correction for the stretching effect, closed loop focus control and always better throughput. One of the main limitations in simultaneous confocal images and Raman spectra is the interference noise in the circulator. Future versions of the light launch will forego the fiber circulator and instead use a polarization beam splitter between the laser and fiber launch, a polarization maintaining fiber, and the quarter wave plate already in use to provide polarization based discrimination of input and reflected light. This technique should eliminate the interference noise from the circulator and allow enough power to reach the sample for Raman sampling without any adjustments of the light launch. An investigation into other objective lenses, such as water immersion objectives, could prove useful. It is our goal that all of these aspects will be incorporated into the next generation CIRSM.

REFERENCES CITED

[1] S. Sigurdsson, P. A. Philipsen, L. K. Hansen, J. Larsen, M. Gniadecka, H. C. Wulf. Detection of skin cancer by classification of raman spectra. *IEEE Transactions on Biomedical Engineering*, 51(10):1784 – 1793, 2004.

[2] Ahmedin Jemal et al. Cancer statistics, 2004. *CA: A Cancer Journal for Clinicians*, 57:43–66, 2004.

[3] S. Presser, J. Taylor. Clinical diagnostic accuracy of basal cell carcinoma. *Journal of the American Academy of Dermatology*, 16:988990, 1987.

[4] Bernt Lindelöf, Mari-Anne Hedblad. Accuracy in the clinical diagnosis and pattern of malignant melanoma at a dermatological clinic. *The Journal of Dermatology*, 21:461464, 1994.

[5] K. C. Nischal, Uday Khopkar. Dermoscope. *Indian J Dermatol Venereol Leprol*, 71(4):300–303, July 2005.

[6] C. V. Raman, K. S. Krishnan. A new type of secondary radiation. *Nature*, pages 501–502, March 1928.

[7] Herman A. Szymanski. *Raman Spectroscopy: Theory and Practice*. Plenum Press, 1967.

[8] P. J. Caspers, G. W. Lucassen, G. J. Puppels. Combined in vivo confocal raman spectroscopy and confocal microscopy of human skin. *Biophysical Journal*, 85:572–580, July 2003.

[9] Milind Rajadhyaksha, Salvador González, James M. Zavislan, R. Rox Anderson, Robert H. Webb. In vivo confocal scanning laser microscopy of human skin II: Advances in instrumentation and comparison with histology. *The Journal of Investigative Dermatology*, 113(3):293–303, September 1999.

[10] Peter J. Caspers, Gerald W. Lucassen, Elizabeth A. Carter, Hajo A. Bruining, Gerwin J. Puppels. In vivo confocal raman microspectroscopy of the skin: Noninvasive determination of molecular concentration profiles. *The Journal of Investigative Dermatology*, 116(3):434–442, March 2001.

[11] Wikipedia. Skin. http://en.wikipedia.org/wiki/Skin.

[12] Sacher Lasertechnik. Spectroscopy with diode lasers. http://data.sacher-laser.com/techdocs/dlspec.pdf.

[13] Kaiser Optical Systems Inc. Holospec f/1.8i holographic imaging spectrograph. http://www.kosi.com/Raman_Spectroscopy/holoSpecf18i.php?ss=600.

[14] Gordon S. Corle Timothy R., Kino. *Confocal Scanning Optical Microscopy and Related Imaging Systems*. Academic Press, 1996.

[15] Philip C. D. Hobbs. *Building Electro-Optical Systems: Making It All Work*. John Wiley & Sons, Inc., 2000.

[16] M. Gu, C. J. R. Sheppard, X. Gan. Image formation in a fiber-optical confocal scanning microscope. *Journal of the Optical Society of America A*, 8:1755–1761, November 1991.

[17] D. L. Dickensheets. *A microfabricated scanning confocal optical microscope for in situ imaging*. Doctoral Dissertation, Stanford University, 1997.

[18] J.F. Aitken, M. Janda, M. Elwood, P.H. Youl, I.T. Ring, J.B. Lowe. Clinical outcomes from skin screening clinics within a community-based melanoma screening program. *Journal of the American Academy of Dermatology*, 54(1):105–114, 2006.